

Modeling W44 as a Supernova Remnant in a Density Gradient, with a Partially Formed Dense Shell and Thermal Conduction in the Hot Interior

R. L. Shelton^{1,2}, Donald P. Cox¹, Witold Maciejewski³, Randall Smith^{1,4,5},
Tomasz Plewa^{6,7}, Andrew Pawl¹, and Michał Różyczka^{7,8}

May 3, 2019

Abstract

We show that many observations of W44, a supernova remnant in the galactic plane at a distance of about 2500 pc, are remarkably consistent with the simplest realistic model. The model remnant is evolving in a smooth ambient medium of fairly high density, about 6 cm^{-3} on average, with a substantial density gradient. At the observed time it has an age of about 20,000 years, consistent with the age of the associated pulsar, and a radius of 11 to 13 pc. Over most of the outer surface, radiative cooling has become important in the post shock gas; on the denser end there has been sufficient compression of the cooled gas to develop a very thin dense half shell of about $450 M_{\odot}$, supported against further compression by nonthermal pressure. The half shell has an expansion velocity of about 150 km s^{-1} , and is bounded on the outer surface by a radiative shock with that speed.

The deep interior of the remnant has a substantial and fairly uniform pressure, as expected from even highly idealized adiabatic models; our model, however, is never adiabatic. Thermal conduction, while the remnant is young and hot, reduces the need for expansion cooling, and prevents formation of the intensely vacuous cavity characteristic of adiabatic evolution. It radically alters the interior structure from what one might expect from familiarity with the Sedov solution. At the time of observation, the temperature in the center is about 6×10^6 K, the density about 1 cm^{-3} . The temperature decreases gradually away from the center, while the density rises. Farther out where cooling is becoming important, the pressure drops precipitously and the temperature in the denser gas there is quite low. Our model is similar to but more comprehensive than the recent one by Harrus *et al.* (1997). Because their model lacked thermal conduction, ours is more successful in providing the thermal x-rays from the hot interior, including a better match to the spectrum, but neither provides the sharpness of the central peaking without further complications.

By using a 2d hydrocode to follow the evolution in a density gradient, we are able to verify that the spatial and velocity structure of the HI shell are a good match to the observations, without the complications suggested by Koo and Heiles (1995), and to demonstrate that the remnant's asymmetry does not substantially affect the distribution of x-ray emitting material. A 1d hydrocode model is then used to explore the effects of nonequilibrium ionization on the x-ray spectrum and intensity. We calculate the radio continuum emission expected from the compression of the ambient magnetic field and cosmic rays into the dense shell (the van der Laan mechanism, 1962a) and find it to be roughly consistent with observation, though the required density of ambient cosmic ray electrons is about 4 times greater than that estimated for the solar neighborhood. We estimate the optical emission that should be present from fluorescence of UV, emitted by the forming shell and the radiative shock and absorbed in the cold shell and the ambient medium, and the associated $63 \mu\text{m}$ [OI] emission. Both are in agreement with the intensity and spatial structures found in recent observations. Neither requires interaction with a dense molecular cloud for its generation. We calculate the gamma rays that should be emitted by cosmic ray electrons and ions in the shell, interacting with the cold material, and find each capable of generating about 25% of the flux reported by EGRET for the vicinity.

We provide several analytic tools for the assembly of models of this type. We review the early evolution and shell formation analyses and their generalizations to evolution in a density gradient. We also calculate the density and temperature that should be present in the

hot interior of a remnant with thermal conduction. We supply the van der Laan mechanism in a particularly useful form for the calculation of radio continuum from radiative remnants. Finally, we demonstrate a simple technique for estimating the optical emission expected. These tools are employed to choose parameters of models which we then explore with our 1d and 2d hydrocodes, providing, respectively, the detailed x-ray spectra and dynamical characteristics.

**supernova remnants — W44 — cosmic ray acceleration — x-rays — gamma rays
— masers — radio continuum — interstellar matter**

affiliations:

1: Department of Physics, University of Wisconsin-Madison, 1150 University Ave., Madison, WI 53711 USA

2: Laboratory for High Energy Astrophysics, NASA/Goddard Space Flight Center, Greenbelt, MD 20771

3: Department of Astronomy, University of Wisconsin-Madison, 750 Charter St., Madison, WI 53711 USA

4: Laboratory for Astronomy and Solar Physics, Code 685, NASA/Goddard Space Flight Center, Greenbelt, MD 20771

5: Harvard-Smithsonian Center for Astrophysics, 60 Garden St, Cambridge, MA 02138

6: Max-Planck-Institut für Astrophysik, Karl-Schwarzschild-Strasse, 85-740 Garching, GERMANY

7: N. Copernicus Astronomical Center, Bartycka 18, 00-716 Warszawa, POLAND

8: also, Member, Interdisciplinary Center for Mathematical Modelling, Pawińskiego 5a, 02-106 Warszawa, POLAND

e-mail addresses:

RLS = shelton@spots.gsfc.nasa.gov

DPC = cox@wisp.physics.wisc.edu

WM = witold@uwast.astro.wisc.edu

RKS = rsmith@kracko.harvard.edu

TP = tomek@camk.edu.pl

MR = mnr@camk.edu.pl

1 Introduction

W44 (3C392) is a supernova remnant (SNR), located near the Galactic plane ($l = 34.7^\circ$, $b = -0.4^\circ$), which has a centrally peaked distribution of thermal x-ray surface brightness, coupled with a shell-like radio continuum morphology. This combination makes it a member of the SNR class which also includes W28, 3C400.2, Kes 27, MSH 11-61A, 3C391, and CTB1 (Rho 1995).

In this paper we demonstrate that many observed features of this remnant are consistent with the simplest realistic model, a remnant evolving in a fairly smooth ambient medium of moderate density with a substantial density gradient, and with thermal conduction active in its interior. It has a radiative shock and dense shell on one side which is emitting copious amounts of optical and IR radiation, and is sweeping up and compressing ambient cosmic rays and magnetic field to produce radio synchrotron and gamma rays. This interpretation differs substantially from earlier attempts to model the remnant's x-ray emission or 21 cm characteristics as arising from a population of evaporating clouds in the interior or the disruption and acceleration of a wind blown shell, but is similar in spirit to the recent investigation by Harrus *et al.* (1997). Our model differs from the latter in that it includes thermal conduction within the hot interior of the remnant, assesses the effects of the density gradient, and is considerably more detailed dynamically and more ambitious in comparison with observations. Our interpretation also differs from past efforts to understand the radio continuum, the infrared emission, and associated OH masers: we find no evidence for interaction of the remnant with dense molecular clouds in the vicinity.

Section 2 opens with a discussion of the complexity of the region in which W44 is located, followed by a revision in the estimated distance (using a recent rotation curve and the standard galactocentric distance of the Sun). It then surveys the observations of W44, including radio continuum, 21 cm, X-rays, characteristics of the pulsar and its weak nonthermal nebula, optical,

IRAS and ISO observations, magnetic field measurements via polarization of OH masers, and the gamma rays seen with EGRET.

Section 3 supplies the analytic tools for estimating remnant parameters consistent with the observations. It reviews the Sedov and cooling phases for uniform density, provides a means for estimating the effects of thermal conduction on the characteristics of the remnant interior, surveys the anticipated shell characteristics, introduces the radio continuum expected from the van der Laan mechanism, and provides simple tools for estimating the $H\alpha$, $63\ \mu\text{m}$, and gamma ray intensities. It then shows how, using the approximations of Maciejewski and Cox (1998), the remnant parameters can be estimated in the presence of a density gradient, closing with a summary of what can be learned from analytical modeling alone.

Section 4 presents the physical assumptions of the hydrocode modeling and describes their implementation and justification. This includes the use of a nonthermal pressure term, the thermal radiation emissivity and spectrum, and the assumptions regarding dust, thermal conduction, and synchrotron emission.

Section 5 presents the results of 2d modeling, exploring the density, temperature and pressure structures of the hot interior and the mass, velocity, and nonthermal emissivity structures of the dense shell. Extensive comparison is made with both the 21 cm and radio continuum observations. The non-equilibrium ionization could not be followed, but we verified that the structure in the hot interior is nearly spherically symmetric and should be reasonably approximated by the 1d model, which is able to track the ionization of the plasma.

Section 6 presents the results of 1d modeling, aimed principally at obtaining the x-ray surface brightness distribution and its spectrum, and comparison with those observations.

Finally, Section 7 provides the discussion and conclusions.

2 Survey of Observations

The essential observed properties of W44 itself are summarized in Table 1 at the end of this section. Detailed description beyond the survey below can be found in recent papers by Giacani *et al.* (1997), de Jager & Mastichiadis (1997) and Harrus *et al.* (1997).

2.1 Environment

W44 lies in a complex region of the sky, in close proximity to several molecular clouds (Sato, 1986), in a giant molecular cloud (GMC) complex (Dame 1983, Dame *et al.* 1986), and at the base of the Aquila Supershell (Maciejewski *et al.* 1996). The ambient density in which the remnant evolves is fairly high (averaging about $6\ \text{cm}^{-3}$, from our results below), presumably because of its GMC environment. Filamentation of the surface emission shows that the medium is moderately irregular on scales somewhat smaller than the remnant. It has been suggested that the remnant may be impacting directly on a very dense molecular cloud; the interpretation of the clearly associated OH masers by Claussen, *et al.* (1997), for example, is based on that assumption. Our model does not include this possible interaction and appears not to require it to understand any of the other observations. Considering the superbubble and its funnel-like connection to the GMC complex in the galactic plane, it is tempting to suppose that W44 might be the latest of a series of SNe in the general region, the earlier ones having contributed energy to the superbubble. Thus far, there is no evidence for any transport of energy from W44 except by cooling radiation and, possibly, escaping cosmic rays; its high density environment has quite effectively localized the mechanical and thermal components of its energy. Any contribution it may make to the superbubble lies in the future.

2.2 Distance Determination

In order to estimate the distance to the supernova remnant, Caswell *et al.* 1975 measured the 21 cm absorption profile toward W44. They found components at velocities of +12, +22, +30, and +42 km sec^{-1} . (In confirmation, Goss, Caswell, and Robinson (1971) observed 1667 MHz OH absorption components at +12.5, +22, +30, and +42 km sec^{-1} .) Because there are no higher

velocity components, the $+42 \text{ km sec}^{-1}$ component corresponds to the near kinematic distance. Using the Schmidt (1965) galactic rotation curve and 10 kpc as the distance between the Earth and the galactic center, Caswell *et al.* estimated the distance to W44 as 3 kpc. We have recalculated the distance using the Clemens (1985) galactic rotation curve and 8.5 kpc as the distance between the Earth and the galactic center. The new estimate is 2.5 to 2.6 kpc.

2.3 Radio Continuum Observations

W44 appears as an elongated shell-type remnant in radio continuum maps. The size, measured from the Giacani *et al.* (1997) 1442.5 MHz image is $25' \times 35'$. In the less detailed map from the 11 cm survey of Reich *et al.* (1990), the remnant appears noticeably brighter over the eastern half.

The radio continuum image presented by Jones, Smith, & Angellini (1993) shows a very highly filamentary structure indicative of a severely edge brightened distribution of emission. The filaments are concentrated on the eastern side and are contained within a sharp boundary, while the western side contains only one very bright feature and has a muted boundary.

Kundu and Velusamy (1972) show that W44 has a very regular linear polarization pattern. In the brighter half of the source, the polarization reaches 20%, and the magnetic field vector is almost parallel to the long axis of the remnant. The bright filaments tend to lie along this axis as well.

The flux densities have been measured over a wide range of radio frequencies (e.g. by Kundu and Velusamy, 1972; Dickel and DeNoyer, 1975; Clark and Caswell, 1976; Clark, Green, and Caswell, 1975; Kassim, 1992). The spectral index is about -0.33 (Kovalenko *et al.* 1994) to -0.4 (Giacani, *et al.* 1997), the latter reporting a flux density of about 400 Janskys at 330 MHz. Table 1 shows 500 Janskys at 100 MHz as representative.

2.4 HI 21 cm Emission from W44

Koo & Heiles (1995) have made a 21 cm velocity resolved map of W44 and found emission up to $v_{\text{LSR}} = 210 \text{ km s}^{-1}$. By subtracting off the systemic velocity of the clouds in this region ($\sim 43 \text{ km/s}$, Sato 1986), they were able to estimate the shell's expansion velocity as $150 \pm 15 \text{ km s}^{-1}$. The observations at low velocity near the limb were badly confused with ambient material, leaving an accessible velocity range only above 130 km s^{-1} LSR. The atomic hydrogen mass in the shell integrated over this range was about $73 M_{\odot}$. Thus, if the neutral material is confined to a thin shell, the average HI column density of the receding side of the remnant is about $3 \times 10^{19} \text{ atoms cm}^{-2}$. Koo and Heiles searched for the near side of the SNR, but found no emission with $v_{\text{LSR}} < -70 \text{ km s}^{-1}$.

By fitting the profile of an expanding shell to their position-velocity diagrams, Koo and Heiles (1995) estimated the full angular size of the HI distribution from their observations over a restricted velocity range. They concluded that the HI distribution is somewhat smaller than and interior to the radio continuum shell. This conclusion will be disputed in section 5.2.2 below where the spatial distribution and position-velocity diagrams of the HI data are compared directly with our model.

2.5 X-ray Observations

The ROSAT PSPC (Rho *et al.*, 1994) and *Einstein* IPC (Smith *et al.*, 1985) x-ray maps show centrally concentrated thermal emission whose dim outer edge extends as far as the radio continuum shell in the north, south, and west (Rho *et al.* 1994). (This appearance, however, may be due in part to scattering of the x-rays by the substantial column density of dust along the line of sight.) The X-ray emitting region may similarly extend to the eastern edge where it is absorbed by a foreground molecular cloud which covers irregularly from $\alpha(1950) \cong 18^{\text{h}}53^{\text{m}}40^{\text{s}}$ to $18^{\text{h}}54^{\text{m}}55^{\text{s}}$ and $\delta(1950) \cong 01^{\circ}10'$ to $01^{\circ}20'$ (Wootten, 1977). Rho *et al.* (1994) separately analyzed 11 spatial zones in the ROSAT PSPC image. From fitting the pulse height distribution with equilibrium ionization thermal models, they found values for the temperature of the X-ray emitting gas from 3.9 to $7.6 \times 10^6 \text{ K}$. The fitted values for the column density of intervening absorbers ranged from 1.6 to $2.1 \times 10^{22} \text{ cm}^{-2}$. From the spatial distribution of these results they conclude that there is no significant radial trend in temperature. Working from the fitted results is somewhat misleading,

however, as Figure 7 of Rho *et al.* (1994) clearly shows that the spectral hardness is significantly greater in the center where the x-rays are brightest.

Smith *et al.* (1985), Jones *et al.* (1993), and Rho *et al.* (1994) calculated the x-ray luminosity for the remnant interior from the *Einstein*, EXOSAT, and ROSAT data, respectively. Their estimates should be reduced by about 25 to 30% at our revised distance. The implied emission measure within the remnant requires an rms electron density of about 0.4 to 0.75 cm⁻³.

The details of the observed x-ray surface brightness distribution and spectrum are presented in section 6 where they are compared with the results of our 1d model.

2.6 The Pulsar and its Synchrotron Nebula

An apparently associated 267 millisecond pulsar (PSR B1853+01) lies projected on the southern part of the remnant (Wolszczan, Cordes, and Dewey 1991). Its age ($\sim 20,000$ years $\pm 20\%$) provides an estimate for that of W44, and is typical of radiative remnants. The pulsar powers a small synchrotron nebula, observed in 4.0 to 9.5 keV ASCA data (Harrus, Hughes, and Helfand, 1996), and in 4860 and 8440 MHz VLA data (Frail, Giacani, Goss, and Dubner, 1996). The x-ray flux from synchrotron is much smaller than the thermal component.

2.7 Optical

Giacani *et al.* (1997) have taken H α and [SII] images of W44. All observed optical emission is within the boundaries of the radio shell, but at the sensitivity of the observation is not found everywhere within it. There appears to be noticeably higher foreground extinction in the south. The brightest H α features have a surface brightness $\sim 1 \times 10^{-16}$ ergs cm⁻² s⁻¹ arcsec⁻² while the faintest features visible in the image have about a tenth that. The brightness of the [SII] lines is not reported but the exposure time was the same and the image showed comparable structure leading us to believe that the intensity is similar. Much of the optical emission is filamentary and in excellent correlation with radio continuum filaments. In some places there is fairly bright H α that is smoother and not well correlated with the radio. On the eastern half of the remnant, where the radio is generally brighter, the observable optical emission is much lower. The H α features correlate with [SII] emission, which often traces radiative shocks. Conversely, the spatial correlation between the optical and x-ray emission is poor, even on very large scales, differing entirely from what would be expected if the H α and [SII] emission arose from evaporating clouds which were loading the interior with mass and enhancing the density of hot gas.

2.8 Infrared, OH Masers, and Gamma Rays

Giacani *et al.* (1997) show IRAS observations in 60 and 100 μ m in a large field around W44, which they say indicate emission compatible with an origin in shock heated dust, while ISO observations presented by Reach and Rho (1996) indicate that, in all fields they examined, the continuum is characteristic of dust heated by the diffuse interstellar radiation field and is dominated by pre-shock and unrelated clouds. The IRAS map, however, shows weaker emission interior to the northern and mid-southern sections of the remnant not explored by ISO, that may well arise from hot dust within the remnant. (The ISO sampling crossed the southern edge of the northern enhancement, and Reach and Rho report that the continuum is brighter there and peaked at the edge where there is a radio ridge, but make no further comment about the heating mechanism.)

Reach & Rho (1996) also observed bright [OI] 63 μ m emission, particularly enhanced on the edge of the remnant where their cut crossed a radio filament, but everywhere higher within the remnant than outside. They quote their peak surface brightness as 10⁻³ erg cm⁻² sr⁻¹ (presumably also s⁻¹), and estimate the total luminosity of the remnant in this line at $\sim 1000 L_{\odot}$. This line is an important coolant in shocked gas, but after an unsuccessful attempt to model it as shock emission, they interpreted it as evidence that W44 is interacting with a dense molecular cloud, even though the region explored does not appear from the IRAS maps to be abutting a dense cloud, being well northwest of that explored by Wootten (1977), for example. In Section 3.5, we show that the [OI] 63 μ m emission is in fact quantitatively consistent with our model, involving no interaction with dense molecular material.

As mentioned previously, the OH masers observed by Claussen *et al.* (1997), were also interpreted as being collisionally excited by the SNR shock passing through a molecular cloud. They point out that DeNoyer (1983) contradicted the early evidence for such interaction, but then cite the [OI] observations just discounted as the strongest independent evidence for it.

Claussen *et al.* (1997) were further influenced by the presence of an unidentified EGRET gamma ray source error circle overlapping the eastern limb of W44, suggesting that it may be due to cosmic rays from W44 interacting with an abutting dense cloud. The Wooten cloud is in fact projected on that location and Esposito *et al.* (1996) show that the source brightness, 50×10^{-8} photons $\text{cm}^{-2} \text{s}^{-1}$ above 100 MeV, would require a cosmic ray intensity within the cloud nearly 100 times ambient, even if the entire cloud is being irradiated.

3 Analytic Modeling

3.1 Overview of the The Basic Model

In combination, the radio continuum and 21 cm observations provide a persuasive qualitative picture of this object. The strong filamentation of the radio continuum is characteristic of that from the very thin dense shell on the surface of a radiative remnant. The radio continuum maps, with their concentration toward (and sharp edge on) the east, and elongation southeast to northwest, give the impression of an emitting surface that is incomplete, somewhat like half an egg shell with the open end roughly toward the west or southwest. The 21 cm emission is also suggestive of an incomplete shell, with the observable part in recession.

For our model, we adopt this qualitative picture, assuming that evolution is occurring in a medium that is denser on the northeast far side, that shell formation has occurred, but only on the denser end, and that the filamentation is indicative of irregularity (corrugation) in the shell's surface, as explored for optical filamentation by Hester (1987). A schematic of the model is shown in Figure 1.

Our choice of northeast to southwest, orthogonal to the observed major axis, for the projected axis of the density gradient requires a bit of explanation. We had initially expected that the density gradient would provide the elongation of the remnant, and that we should be taking the gradient along the elongation. When we became more familiar with the Kompaneets Approximation (Maciejewski and Cox, 1998), however, we discovered that in an exponential density distribution a remnant remains nearly spherical much longer than we had expected. It expands more rapidly in directions of lower density, but the effect is to displace the center of the sphere down the gradient from the explosion site, not to elongate the envelope. Eventually we realized that a partial shell capping one end of a sphere could appear elongated, but that the elongation would be transverse to the density gradient. For this reason we have adopted the observed semimajor axis as the remnant radius, and taken the model gradient orthogonal to it.

The remnant characteristics, summarized in Table 1 can be combined in a variety of ways to demonstrate that W44 must indeed be a supernova remnant, with an explosion energy of about 10^{51} ergs. For brevity we will adopt this result and from it derive the remnant characteristics assuming the age to be 20,000 years, the nominal age of the pulsar. There are two free parameters, the density at the explosion site and the scale height of the density distribution.

Determination of these two parameters follows from three requirements: (1) that shell formation has occurred on the dense end and extended about half way around the remnant to the equator, that (2) there be sufficient mass already in the half shell to explain the amount seen in 21 cm, but (3) with a shell expansion velocity as large as that seen.

In the remainder of this section, we determine these parameters and make analytic predictions for the basic structure (the remnant radius, shell expansion velocity, edge temperature, central pressure, central density and temperature, shell density and magnetic field), and for anticipated characteristics in observed emission modes (thermal X-rays, radio synchrotron, $\text{H}\alpha$, $63 \mu\text{m}$, and gamma rays).

Characteristic	Value	Observation	Notes
SNR Angular Size	25' × 35'	Radio Continuum	
Observed Shape	Pearlike	Radio Continuum	
Elongation	Northwest-Southeast		
Evolutionary Stage	Partial Shell Formation	HI Emission	1
Model Axis	Northeast-Southwest		2
Distance	2.5 to 2.6 kpc	HI, OH Absorption	3
Radius	~ 11 to 13 pc		
Age	~ 20,000 years	Pulsar	
Radio Continuum Flux Density	~ 500 Jansky @ 100 MHz		
Spectral Index	~ 0.33 to 0.4	Radio Continuum	
Shell Expansion	150 ± 15 km sec ⁻¹	HI Emission	
Shell N _H	~ 3 × 10 ¹⁹ cm ⁻²	HI Emission	
Optical Configuration	filamentary, within radio remnant	H α , [SII]	
Peak H α surface brightness	~ 1 × 10 ⁻¹⁶ ergs cm ⁻² s ⁻¹ arcsec ⁻²		
Peak 63 μ m surface brightness	10 ⁻³ erg cm ⁻² sr ⁻¹ s ⁻¹	ISO	
63 μ m luminosity	~ 1000 L _⊙		
Gamma-Ray Source Box	includes eastern limb		
Gamma-Ray Flux above 100 MeV	50 × 10 ⁻⁸ photons cm ⁻² s ⁻¹	EGRET	
X-Ray Morphology	Centrally Bright, No Shell	0.2 to 4 keV X-ray	4
	Extends Dimly to Radio Boundary		5
X-Ray Emission Mechanism	Thermal	Observable Lines	
Central Temperature	~ 4 – 8 × 10 ⁶ K	X-ray	
Interior n _e	~ 0.4 to 0.75 cm ⁻³	X-ray	6
Central Pressure	~ 1.4 × 10 ⁻⁹ dyn cm ⁻²	X-ray	
Absorption N _H	~ 1.6 – 2.1 × 10 ²² cm ⁻²	X-ray	
Pulsar Nebula	Unimportant in 0.2 to 2 keV	4 - 9.5 keV, 20 cm	

Table 1: Quantities derived from the observations: Note 1: The dense shell formation is more fully developed on the northeast rear section; Note 2: The model axis is assumed perpendicular to the elongation in radio continuum emission because the shell is partial; Note 3: This is a new distance estimate. Note 4: Harrus *et al.* 1996 present a 0.5 to 4.0 keV image which shows the central brightening, as does Rho *et al.*'s (1994) ROSAT data. Note 5: The dim envelope of the x-ray emission extends to the boundary in most directions. Note 6: The reported electron densities have been scaled by 1.07 to reflect a change in the assumed distance from 3000 pc to 2600 pc.

3.2 Review of Shell Formation in a Homogeneous Medium

In our notation, n and n_e refer to the densities of nuclei and electrons, respectively. Then $n = n_H + n_{He} = 1.1n_H$, where n_H and n_{He} are the densities of hydrogen and helium nuclei, and $n_{He}/n_H = 0.1$ is assumed. In this notation, the mass density is $\rho = mn$, where the average mass per nucleus is $m = (1.4/1.1)m_H$, m_H being the mass of hydrogen. The perfect gas law, assuming equal electron and ion temperatures is then $p = \chi nk_B T$, where $\chi = (n + n_e)/n$. For neutral gas, χ is 1, for fully ionized it is (2.3/1.1).

The Sedov self similar structure and evolution yield several useful results for middle aged remnants if the effects of cooling have not yet been large. The shock radius is $R_s = [2.025E_o t^2 / (mn_o)]^{1/5}$ where E_o is the explosion energy and n_o is the ambient value of n , assumed uniform. The shock velocity is then $v_s = dR_s/dt = (2/5)R_s/t$. From the jump conditions, the post shock density is $4n_o$, the pressure is $p_s = [3/4]mn_o v_s^2$, and from the perfect gas law in our notation, the post shock temperature is $T_s = (3/16)mv_s^2/(\chi k_B)$. In addition, the pressure in the center of the remnant is $p_C \approx 0.31p_s$.

Kahn (1975, 1976) introduced a very useful approximation technique for estimating the cooling timescale for supernova remnants. In that approximation, the cooling coefficient takes the form $L = \alpha_{Kahn} T^{-1/2}$. It has the special property that in the absence of thermal conduction, the time for a parcel of hot gas to cool from an initial state is independent of its history and equals

$$\Delta t_{cool} = \frac{p_s}{Ln^2}. \quad (1)$$

For a newly shocked parcel of gas, p, T , and n are known and thus, so is Δt_{cool} . To find the actual time t_{finish} at which the parcel will finish cooling, the post shock cooling time must be added to the time t_{shock} at which the parcel is first shocked ($t_{finish} = t_{shock} + \Delta t_{cool}$). To find the time at which the first parcel cools, the minimum is found for the function $t_{finish}(t_{shock})$. This minimum is the cooling time for the remnant, t_{cool} . Details appear in Cox and Anderson (1982) and Cox (1986).

The cooling time, however, should not be confused with the shell formation time t_{shell} . The first gas which cools in a remnant does so rapidly. It drops to a very low pressure relative to its surroundings, and is only later compressed and repressurized by flows of cooling gas from both sides, these driven by the pressure differential. It is therefore not correct to assume that ‘‘cooling’’ and ‘‘compression’’ (i.e. dense shell formation) proceed simultaneously. From experiments with hydrocodes, we estimate that $t_{shell} \approx (7/6)t_{cool}$. The result, and numerical forms with $\alpha_{Kahn} = 1.3 \times 10^{-19}$ cgs, are

$$t_{cool} \approx 0.208 \left[(m^{9/14} E_o^{3/2}) / [\alpha_{Kahn}^{5/2} (\chi k_B)^{5/4} n_o^4] \right]^{1/7} \quad (2)$$

$$t_{cool} \approx 45.5 \times 10^3 \text{ years } E_{51}^{3/14} / n_o^{4/7} \quad (3)$$

$$t_{shell} \approx 53 \times 10^3 \text{ years } E_{51}^{3/14} / n_o^{4/7}. \quad (4)$$

We are now in a position to estimate the remnant’s dynamical characteristics at the moment when shell formation reaches the equator, and to make an initial estimate of the ambient density, by solving for the epoch at which $t_{shell}(E_o, n_{avg})$ equals the remnant age, about 20,000 years. Including the possibility that the age or explosion energy are probably not exactly our nominal values, the values for shock radius, shell velocity, and central pressure when the shell formation time equals the age, and the required average density are (with $t_{20} = t/(20,000 \text{ yr})$)

$$R_s \approx 12 \text{ pc } E_{51}^{1/8} t_{20}^{3/4} \quad (5)$$

$$v_{shell} \approx 0.75v_s \approx 176 \text{ km s}^{-1} E_{51}^{1/8} / t_{20}^{1/4} \quad (6)$$

$$p_C \approx 0.31p_s \approx 1.5 \times 10^{-9} \text{ dyn cm}^{-2} E_{51}^{5/8} / t_{20}^{9/4} \quad (7)$$

$$n_o \approx 5.5 \text{ cm}^{-3} E_{51}^{3/8} / t_{20}^{7/4} \quad (8)$$

These are the (approximate) anticipated conditions at the moment when shell formation first occurs, a condition which we believe applies at the equator of W44. The remarkable fact is that

even at the nominal values of explosion energy and age, the radius and central pressure are easily within the observational uncertainties. The shell velocity is somewhat high, but we expect a lower velocity toward the denser end where the shell is more completely developed, and which in our projection is closer to the line of sight. Further insight derives from evaluating the temperature that would have been at the edge of the remnant had there been no cooling, considering it to be an estimate of the temperature of hot gas at the outer edge of the hot interior (just interior to the dense shell) at this epoch. The result is $T_{\text{outer}} \approx 7.6 \times 10^5 \text{ K } E_{51}^{1/4} / t_{20}^{1/2}$. As found by Harrus *et al.* (1997), the remnant edge at this epoch is somewhat too cool to provide a strong shell source of X-rays.

There is another consistency check in the HI column density, about $3 \times 10^{19} \text{ cm}^{-2}$ from Table 1. If all the mass in a sphere is swept into a thin shell at the edge, the perpendicular column on one side should be $n_o R_s / 3$. This is about $7 \times 10^{19} \text{ cm}^{-2}$ for our parameters, a consistent value considering the uncertainty in the observations, the recency and incompleteness of shell formation, and the unknown fraction of the mass that is molecular. If the observed HI arises from any other cause, it would be exceedingly unlikely for it to have the column density and expansion velocity expected for the cooled SNR shell. Making the details of the shell mass work out correctly depends only on making the correct choice for the density scale height, a topic we defer until after considering the effects of thermal conduction on the central density and temperature of the remnant.

3.3 The Central Density and Temperature

As we have suggested in the introduction and shown elsewhere (Slavin and Cox, 1992, Cui and Cox, 1992, and Shelton, Smith, and Cox, 1995), thermal conduction in the hot interior of a remnant prevents formation of the vacant interior characteristic of nonconductive evolution. Transporting heat away from the remnant interior lowers the specific entropy and therefore the expansion rate needed to accommodate the falling pressure, thereby moderating the extraordinary reduction in central density found in models ignoring conduction. The central pressure remains uniform at about 0.3 of that at the edge, but the temperature and density are also made nearly uniform as well. In this section we show that this effect can provide the conditions found in the x-ray emitting interior of W44.

There is considerable concern, of course, that thermal conduction might be very heavily suppressed, and/or anisotropic in supernova remnants due to the magnetic field. We have addressed this point previously (Slavin and Cox, 1992, and Cox, 1996) but, in light of its importance to our present application, discuss it somewhat further in section 4.4.

Experience with hydrocodes has suggested that the central density n_c at the epoch of shell formation, in a remnant with unsuppressed conduction, is roughly $0.1n_o$. We have previously shown (Shelton, Smith, and Cox, 1995) that this factor of 10 density contrast between the interior and the ambient medium can be understood analytically, and elaborate on that result now, exploring its dependence on the magnitude of the thermal conductivity.

Cui and Cox (1992) developed a similarity solution for conduction that made it possible to estimate a remnant's central adiabat, temperature, and density analytically for times in the vicinity of the cooling epoch. There was unfortunately a typographical error; the density exponent in their equations (A17) and (39) should be 208/225. In addition, the units are incorrectly described just before (39) but are correct in their appendix. The generalization of the coefficient B in their equation (A14), to find the dependence on the magnitude of the conductivity, is

$$B = 29.2 \beta m^{12/25} n_o^{208/225} / [(\chi k_B)^{7/2} E_o^{26/75}] \quad (9)$$

where the classical conductivity is taken as $\beta T^{5/2}$, with $\beta \sim 6 \times 10^{-7} \text{ cgs}$.

With this result, and assuming the Kahn cooling function, the ratio of the central to ambient density turns out to be independent of explosion energy or ambient density. The value and form are,

$$n_c/n_o = 0.334 q^{18/71} (t_{\text{cool}}/t)^{18/25} \left[(t/t_{\text{cool}})^{1/25} - (0.44q^{5/14})^{1/25} \right]^{18/71}, \quad (10)$$

with $q \equiv 145m\alpha_{\text{Kahn}}\beta/(\chi k_B)^3$ (defined so that $q = 1$ for full conduction and normal cooling rates). For $t = (7/6)t_{\text{cool}}$, as at shell formation, and $q = 1$, we find $n_c/n_o \approx 0.13$, nicely in agreement

with hydrocode experience. Equation 10 probably does not successfully describe time dependence, but should provide a guide to the dependence on conductivity. It predicts the central density to be proportional to $\beta^{0.253}$. A factor of 10 reduction in conductivity should lead to only a factor of 1.8 reduction in the central density and increase in central temperature.

With $n_o \approx 5.5 \text{ cm}^{-3}$, and $q = 1$, we expect a central density within the remnant cavity of $n_c \approx 0.7 \text{ cm}^{-3}$, just the level found from the x-ray surface brightness of W44 (compare with the x-ray results for the central density in Table 1). As the central pressure was shown in the previous section to be at the correct level, the temperature will be appropriate also, roughly $7 \times 10^6 \text{ K}$. We can therefore be confident that conduction will lead to x-ray emission similar in characteristic temperature and emission measure to that seen. We defer to the hydrocodes, however, to learn whether the spectral details in the presence of nonequilibrium ionization, and the radial profile of the surface brightness are also well approximated.

3.4 The Radio Continuum

3.4.1 Evaluation of The Contribution of the van der Laan Mechanism

There is considerable interest in the possibility that the bulk of the cosmic rays arise from diffusive shock acceleration in supernova remnants, an interest which is encouraged by their powerful non-thermal emission (Ellison *et al.* 1994). Before assuming that diffusive shock acceleration plays the dominant role in an evolved supernova remnant which is bounded by a radiative shock, however, it is important to consider the synchrotron emission that would arise from swept up ambient cosmic ray electrons, adiabatically compressioned into the dense shell and radiating in the compressed ambient magnetic field (van der Laan, 1962).

Neglecting small inefficiencies due to misalignment and isotropization, a co-moving relativistic particle in a region compressed by a factor x would have its energy betatron-enhanced (2d adiabatic compression) by about a factor of $x^{1/2}$. The net effect for a supernova remnant with a cooled shell of mass M and original density ρ_o is that cosmic ray electrons previously occupying a volume M/ρ_o of interstellar space find themselves compressed into a shell whose volume is x times smaller, enhanced in their energies by a factor of $x^{1/2}$, and radiating in a magnetic field about x times higher. The characteristic frequency of synchrotron emission of an electron of energy E in a field of strength B is proportional to BE^2 , and is therefore a factor of x^2 higher. Similarly, the total power per electron, proportional to $(BE)^2$, is raised by a factor x^3 . For a distribution of electrons radiating synchrotron with an emission spectrum $A\nu^{-\alpha}$ per electron before compression, the spectrum per electron after compression is $A'\nu^{-\alpha}$, with $A' = x^{1+2\alpha}A$, for a total gain at fixed frequency of $G(x) = x^{1+2\alpha}$.

If one is willing to make assumptions about the isotropy of the particle distribution before, during, and after the acceleration, then this estimate can be made somewhat more precise. For example, assuming an initially random distribution of pitch angles and the post acceleration re-randomization, the overall gain per electron from van der Laan (1962) is

$$G(x) = x^{1+\alpha} \left[\frac{1}{2} + \frac{1}{2} \frac{x}{(x-1)^{1/2}} \sin^{-1} \left(\frac{x-1}{x} \right)^{1/2} \right]^{2\alpha}. \quad (11)$$

Compared with the previous estimate, the numerical difference is slight (here $G(x) \approx (\pi/4)^{2\alpha} x^{1+2\alpha}$ at large x).

Therefore, except for the required units conversions, the flux density of the remnant's radio continuum from this mechanism is

$$S(\nu) = G(x)V_o\epsilon_o(\nu)/d^2, \quad (12)$$

where $V_o = M_{\text{shell}}/\rho_o$ is the shell volume before compression, $\epsilon_o(\nu)$ is the synchrotron emissivity of the ambient ISM at frequency ν , x is the shell compression factor, and $G(x)$ is the gain as given above. The next few paragraphs assemble these parameters.

From the observations summarized in Table 1 and the subsequent modeling, we have estimated the shell radius at 11 to 13 pc, the shell formation process complete over half that surface, the one sided surface density at $3 \times 10^{19} \text{ cm}^{-2}$, and the initial density at 6 cm^{-3} . Thus, the mass of material now in the half shell is about $300 M_\odot$ and its initial volume about $V_o = 1600 \text{ pc}^3$.

W44 has been studied between about 10^2 and 10^4 MHz. Unfortunately, prior to their being swept up by the remnant, the responsible electrons radiate only below 10 MHz where their study is difficult. Thus, the ambient emissivity must be evaluated at the lowest observable frequencies and then extrapolated into the frequency range observed in the remnant. Webber *et al.* (1980) and Rockstroh and Webber (1978) conclude that the data available appear to be consistent at the lowest frequencies with an ambient interstellar synchrotron emissivity of roughly

$$\epsilon_o \sim 1.5 \times 10^{-40} [\nu/30(\text{MHz})]^{-.57} \text{ W}(\text{m}^3 \text{ sr Hz})^{-1}, \quad (13)$$

with apparently real place to place variability. Extrapolation to 100 MHz then yields

$$\epsilon_o(100 \text{ MHz}) \sim 0.8 \times 10^{-40} \text{ W}(\text{m}^3 \text{ sr Hz})^{-1} \quad (14)$$

The fact that the emission spectrum quoted above, with $\alpha = 0.57$, is steeper than the observed spectrum for W44 requires further elaboration. It is attached to the conclusion of Webber *et al.* (1980) that the ambient electron particle index $(1+2\alpha)$ is 2.14 between 70 and 2500 MeV. But they further conclude that below 70 MeV the particle spectrum flattens toward an index of 1.6. In the shell of W44, the emission at 100 MHz derives from electrons with energies about 250 MeV, but prior to compression into the shell the energies of the same electrons would have been 7 to 10 times lower, or roughly 30 MeV. As these electrons are in fact in the flattened part of the spectrum, a spectral index lower than 0.57 but greater than 0.3 (corresponding to particle index 1.6) is expected. Therefore the observed spectral index of W44, 0.33 to 0.4, is nicely consistent. There should be a gradual steepening of the radio spectrum at high energies, but the observability is complicated by the distribution of compression factors within the remnant shell.

This spectral curvature complicates the simple analysis we have undertaken. We have elected to use an intermediate effective index, $\alpha_{\text{eff}} = 0.5$, in evaluating the gain, both because it represents the overall increase in the number of suitable radiating electrons better than the observed indices of W44 or the ambient ISM, and because it leads to a very nice summary formula for the predicted flux density. We expect this simplification to provide an estimate which is reliable to within a factor of two except for remnants with very flat radio spectra. Our adopted approximation for the gain is therefore

$$G(x) \approx \frac{\pi}{4} x^2. \quad (15)$$

In attempting to estimate the compression factor in the shell, we make use of the fact that with either analytic approximations or hydrocode models, it is the total pressure in the dense shell that is its best known characteristic. Then, making assumptions about the thermal, magnetic, and cosmic ray contributions, the corresponding compression factor can be determined.

In the Sedov solution, the pressure at the densest part of the edge is about 3.3 times higher than the central pressure. When cooling sets in, the thermal pressure near the edge drops precipitously at first and then recovers somewhat as neighboring material compresses the cooled gas. On the dense side of W44, the pressure in the dense shell should have recovered in this way, but to a somewhat lower value than for a Sedov remnant which had had no cooling. Cox (1972) suggested that the shell velocity would probably be about the same as the post shock velocity just before cooling, leading to a shell pressure that is 3/4ths of the precooling edge pressure. With this guidance, we estimate that the shell pressure in W44 is now about twice the central pressure p_c , where from Table 1, we have $p_c \sim 1.4 \times 10^{-9} \text{ dyn cm}^{-2}$.

For an overall compression factor x , the thermal pressure in the dense shell will be $(\chi k_B n_o T_f)x$, where T_f is the temperature in the shell. The final temperature is not well known, but assuming $T_f \sim 1000 \text{ K}$, and $\chi = 1$ provides a reasonable estimate in the neutral gas. With $n_o \approx 6 \text{ cm}^{-3}$, the thermal pressure in the shell is negligible compared to the nonthermal terms treated next.

In the shock and subsequent compression into the shell, it is expected that the tangential component of the magnetic field will increase in proportion to the density. As a rough approximation (also used in our hydrocodes), we take the field as effectively transverse everywhere, in which case the magnetic pressure is $x^2 B_{o\perp}^2 / (8\pi)$. We consider values of $B_{o\perp}$ in the range 2 to 5 μG to be plausible.

The pressure due to the compressed ambient cosmic ray electrons is negligible, but the ions could well be important. Their ambient pressure is comparable to that of the magnetic field and their

non-relativistic component will have its pressure increasing approximately as x^2 , like the magnetic pressure, so long as they do not isotropize during the compression. Thus, their contribution to the shell pressure, after strong compression, could be comparable to the magnetic pressure. It can be substantially less if the cosmic ray ions are not efficiently localized (i.e. they leak out) or greater if they are accelerated by more than just the compression. In what follows, the cosmic ray pressure is taken as $p_{\text{CR}} = \beta p_{\text{B}}$, where β is expected to be in the range 0 to 1.

The total pressure is thus approximately $(1 + \beta)x^2 B_{\text{o}\perp}^2 / (8\pi)$ which must equal p_{shell} , yielding an estimated compression factor of

$$x \approx \frac{90}{(1 + \beta)^{0.5}} \left(\frac{3\mu\text{G}}{B_{\text{o}\perp}} \right) \quad (16)$$

which ranges from 40 to 130 over the ranges of β and B_{o} . The implied range of shell density is 220 to 800 cm^{-2} . The magnetic field within the shell is less uncertain, ranging from 185 to 260 μG , depending only on β .

This result can be generalized to any remnant with known shell expansion speed and preshock density, realizing that what we have done is to equate the nonthermal pressure in the shell with the ram pressure of the radiative shock, $p_{\text{ram}} = \rho_{\text{o}} v_{\text{shell}}^2$, yielding

$$x^2 \approx \left(\frac{8\pi}{1 + \beta} \right) \left(\frac{\rho_{\text{o}} v_{\text{shell}}^2}{B_{\text{o}\perp}^2} \right), \quad (17)$$

$$x \approx \left(\frac{90}{(1 + \beta)^{0.5}} \right) \left(\frac{3\mu\text{G}}{B_{\text{o}\perp}} \right) \left(\frac{n_{\text{o}}}{6 \text{ cm}^{-3}} \right)^{1/2} \left(\frac{v_{\text{shell}}}{150 \text{ km s}^{-1}} \right). \quad (18)$$

$$(19)$$

Thus, with $\alpha_{\text{eff}} = 0.5$, the gain can be written

$$G(x) \approx \frac{\pi}{4} x^2 \approx \left(\frac{2\pi^2}{1 + \beta} \right) \left(\frac{\rho_{\text{o}} v_{\text{shell}}^2}{B_{\text{o}\perp}^2} \right), \quad (20)$$

the initial volume of material in the shell as

$$V_{\text{o}} = \frac{M_{\text{shell}}}{\rho_{\text{o}}} = 1600 \text{ pc}^3 \left(\frac{M_{\text{shell}}}{300 M_{\odot}} \right) \left(\frac{6 \text{ cm}^{-3}}{n_{\text{o}}} \right), \quad (21)$$

and the resulting synchrotron flux density as

$$F \approx \left(\frac{2\pi^2 M_{\text{shell}} v_{\text{shell}}^2 \epsilon_{\text{o}}}{(1 + \beta) B_{\text{o}\perp}^2 d^2} \right) \quad (22)$$

or

$$F \approx \left(\frac{500 \text{ Janskys}}{1 + \beta} \right) \left(\frac{\epsilon_{\text{o}}}{10^{-40} \text{ W}/(\text{m}^2 \text{ Hz sr})} \right) \left(\frac{M_{\text{shell}}}{300 M_{\odot}} \right) \left(\frac{3 \mu\text{G}}{B_{\text{o}\perp}} \right)^2 \left(\frac{v_{\text{shell}}}{150 \text{ km s}^{-1}} \right)^2 \left(\frac{2.5 \text{ kpc}}{d} \right)^2 \quad (23)$$

For comparison, Table 1 shows the measured flux density for W44 at 100 MHz to be about 500 Janskys, within the uncertainties, in complete agreement with this estimate.

3.4.2 Discussion

Our estimate of the magnetic field in the shell of $B_{\text{shell}} \approx 200 \mu\text{G}$ was made before learning of a measurement of the field in W44 by Claussen, *et al.* (1997), who also found of order 200 μG . Their measurement was of polarization of OH masers, was more uncertain than our estimation procedure, and was attributed to quite a different picture of the source region. It is therefore somewhat less satisfying than the numerical coincidence would indicate, but could be appropriate. Their interpretation is that a very slow shock is being driven into an abutting molecular cloud, with a density close to 10^4 cm^{-3} and an ambient field not much smaller than what they measure. But the close association of the OH masers with apparently tangentially moving regions of radio

continuum emission and the fact that the measured fields can be achieved in the remnant shell cause one to question whether a molecular cloud interaction is necessary. Certainly the small compressions involved in their scenario would yield negligible radio synchrotron emission via the mechanism we are investigating.

For densities in the range found for the shell, 220 to 800 cm^{-2} , the recombination time is only a few hundred years, so it is reasonable to expect the dense shell to be mostly neutral and responsible for the observed 21 cm radiation.

With a shell compression factor of roughly 100, the local shell thickness (before any distortions) is less than half a percent of the radius. This implies that the radio synchrotron emission is very highly edge brightened and subject to the high degree of ripple/tangency filamentation described by Hester (1987). We present some simulations of this effect in section 5.2.3.

The synchrotron emissivity estimate above hides a fundamental problem with this approach. We have assumed that the best estimates of the ambient cosmic ray electron population, the synchrotron emissivity, and the tangential field strength are mutually consistent. As discussed by Rockstroh and Webber (1978), the characteristic field strength required for consistency is surely greater than the mean field, with the rms field being more suitable. Results of attempts at consistency depend somewhat on the assumed spectral index, but typically require a characteristic field of about 9 μG . The value of ϵ_0 appropriate for a 3 μG field should then be reduced (for $\alpha_{\text{eff}} = 0.5$) by about a factor of 5. Therefore, the flux density of W44 cannot be matched by the van der Laan mechanism alone unless the ambient CR electron population is about a factor of 3 to 5 larger, depending on the shell mass, than estimated for the solar vicinity. (Alternatively, the anisotropy of the synchrotron radiation formulae may have fooled us). We will return to this subject in discussing the gamma rays anticipated from the shell.

The radio continuum flux predicted from the van der Laan mechanism is similar to that observed, but there is clearly room for contributions or enhancements by additional processes, so long as those processes do not produce a markedly different spectrum. The next three paragraphs discuss some of the possibilities.

Some injection by the shock of new cosmic ray electrons may be occurring. Alternatively, electrons accelerated by the remnant when it was younger, or by the pulsar, may be caught up in shell formation and forced to radiate in the vastly enhanced magnetic field there. One might suppose that the problem with either possibility is that there is no obvious reason for the surface brightness and spectrum to be so close to those found for the van der Laan mechanism and by observation, suggesting that we consider, as below, factors that could enhance the radio synchrotron emission over the above estimate without invoking a totally independent mechanism. But perhaps there is a reason for achieving approximately this result with other mechanisms, namely that our emissivity is basically the equipartition result—if for a given pressure, ambient field, and shell mass we ask for the emission from the usual percentage of electrons associated with cosmic ray ions in equipartition with the shell’s magnetic field, we will have roughly what we have calculated, independent of the details of the acceleration mechanism.

Ambient cosmic ray electrons may receive substantial diffusive acceleration on passing through the adiabatic gas subshock, followed by betatron acceleration during compression into the dense shell. These ambient electrons, apparently having a slightly shallower index than that of newly injected and accelerated ones, will maintain their original spectral index while achieving an average energy boost per particle. From elementary theory, the magnitude of the boost is unknown, but potentially large.

Shell formation offers yet another acceleration possibility. Electrons which attempt to diffuse away from the cold dense shell find themselves continually swept back in because there is approaching flow on both sides: recently swept up ambient material cools rapidly and is added to the shell from the outside, while material just interior to the shell which was heated long ago finally cools and provides a condensation flow to the inside (occasionally accompanied by another weak radiative shock). This two sided flow convergence not only reduces particle losses from the densest region, but offers an as-yet-unexplored site of first order Fermi acceleration.

3.5 The H α , [OI] 63 μ m, and Related Luminosities

A rough estimate of the H α luminosity of the remnant can be made following the methods of Cox (1970, 1972a). There are several factors to consider. Hot material inside the remnant and newly shock-heated material on the outside edge are cooling off, recombining, and joining the dense shell. They contribute directly to H α , but also emit EUV which fluoresces in the neighboring neutral material, shell and ambient, to yield even more H α . A further complication is that fluorescence in the ambient medium is not instantaneous; ionization is effectively stored for a recombination time, which at $n_o \sim 6 \text{ cm}^{-3}$ is about the age of W44.

Because the recombinations in shell and ambient material can be distinguished via both spatial distribution and in velocity, we consider them separately. Following Cox (1972a), we estimate that in cooling from high temperature, approximately 4 ionizing photons are radiated per atom. Assuming that half of these photons escape to ionize the ambient medium, the ionization rate for the surroundings is $2 dN/dt$ and the recombination rate for the shell is $3 dN/dt$ (there being one extra from the recombination of the cooling atom). (Here dN/dt is the rate at which atoms join the shell.) The total number of atoms in the remnant is approximately $n_o V \sim 10^{60}$ (about 1000 M_\odot). Of these, we expect that roughly a third (but see below) have cooled during the ~ 3000 years between t_{cool} and t_{shell} , contributing 4×10^{48} atoms s^{-1} to dN/dt . The rate at which atoms are overtaken by the radiative shock (presently covering half the remnant's surface, of total area A) is $n_o(A/2)v_s \sim 1 \times 10^{48}$ atoms s^{-1} . We thus expect a total of $dN/dt \sim 5 \times 10^{48}$ atoms s^{-1} . Results from our 2d hydrocode (below) show this estimate to be about a factor of 2 too high at present (20,000 yr), with the higher rate more representative of the recent past. Because the ionization level of the ambient medium averages the rate over a substantial time, we take the higher rate for it, yielding 1×10^{49} photoionizations s^{-1} for the last 3000 years. For the shell fluorescence the instantaneous value of dN/dt is more appropriate, yielding 0.8×10^{49} recombinations s^{-1} in the dense shell.

From recombination theory there are approximately 0.6 eV of H α emission per average (Case B) recombination. The shell luminosity in H α from the radiative shock should thus be about 3×10^{36} erg s^{-1} . From the above analysis, however, the total number of atoms presently joining the dense shell, including those from the cooling interior, is 2 to 3 times higher, implying a total H α luminosity of about 7×10^{36} erg s^{-1} . Its spatial distribution and velocity structure should resemble those of the radio continuum and HI shell respectively, with one caveat: because shell formation is presently occurring at the equator of W44, we might expect the emission to be brightest there, rather than in the east or northeast where shell formation has already passed its peak. This equatorial configuration is in fact apparent in Fig 1b of the H α picture of Giacani *et al.* (1997) (who attributed it to enhanced absorption in the east), while their Figure 5 demonstrates the expected strong relationship between the H α and radio continuum enhancements and filamentation.

Our luminosity estimate corresponds to an average surface brightness over the ~ 500 square arcmin of the remnant of 6×10^{-15} ergs $(\text{cm}^2 \text{ s}^1 \text{ arcmin}^2)^{-1}$. The extinction at H α implied by an x-ray absorption column density of about $(1.6 \text{ to } 2.1) \times 10^{22}$, however, is a factor of 600 to 4400, for an observable average of $(0.1 \text{ to } 1) \times 10^{-17}$ ergs $(\text{cm}^2 \text{ s}^1 \text{ arcmin}^2)^{-1}$. Giacani *et al.* (1997) quote their peak observed surface brightness as 10^{-16} ergs $(\text{cm}^2 \text{ s}^1 \text{ arcmin}^2)^{-1}$, with the dimmest observable features at 10^{-17} ergs $(\text{cm}^2 \text{ s}^1 \text{ arcmin}^2)^{-1}$. Their brightest features, a factor of 10 to 100 higher than our average, are strongly enhanced by filamentation; but their dimmer features, a factor of 1 to 10 above our estimate, appear much smoother in the equatorial belt. Given the fact that we expect concentration in that region, and that the large extinction is not only uncertain but likely to be variable, the agreement is as good as can be expected.

Because the recombination time in the ambient medium is long, its luminosity will be lower. There have been a total of roughly 10^{60} ionizing photons captured in the surroundings. Neglecting recombinations, they will ionize a similar number of atoms, which will then recombine with a timescale of 10^5 years / $n_o \sim 1.8 \times 10^4$ years, yielding 0.2×10^{49} recombinations s^{-1} and a luminosity of 2×10^{36} erg s^{-1} . Although the total radiation by the shell is expected to be about 3 times brighter, and enormously higher in surface brightness in restricted regions, the fluorescence in the ambient medium is not inconsequential. The ionized mass should be about 1000 M_\odot , like the mass within the remnant, and extend roughly 3 pc outside (even farther but dimmer on the low density end), with an emission measure exceeding 100 cm^{-6} pc. In the absence of inhomogeneity other than

the density gradient, it should be brightest behind the northeast part of the remnant, where the ambient density is high.

Of course the emission of the cooling gas is not restricted to $H\alpha$. The overall spectrum should be rather similar to that of a radiative shock with a speed of about 150 km s^{-1} . From Model G of Raymond (1976), for example, we expect emission from optical lines of [OIII], [OII], [OI], [NII], and [SII], and near IR lines of [CI] that are comparable in intensity to $H\alpha$. In the infrared, predicted strong lines are [FeII] at $26 \mu\text{m}$, [OI] at $63 \mu\text{m}$, and [NeII] at $12.8 \mu\text{m}$, the first of which is about twice as bright as $H\alpha$, the others about one third. The basic picture is not much different in more recent calculations (although inclusion of proton impact excitation alters the strengths of the infrared lines somewhat). Essentially all shock models in the velocity range 130 to 160 km sec^{-1} yield 1 to 3 eV of $H\alpha$ and 0.5 to 1 eV of $63 \mu\text{m}$ emission per average atom through the shock. Once again assuming that the radiation by material joining the dense shell from inside is similar in spectrum to the radiative shock, we conclude that the luminosity in any of the above lines should be about $(3 \text{ to } 10) \times 10^{36} \text{ erg s}^{-1}$. The [SII] was observed by Giacani *et al.* (1997), with a distribution (and presumably intensity, though it was not discussed) similar to that of $H\alpha$. The $63 \mu\text{m}$ line was measured with the ISO LWS by Reach and Rho (1996); from the regions they sampled they estimate a total luminosity of about $10^3 L_\odot$, in excellent agreement with our estimate.

Interestingly, Reach and Rho considered a radiative shock model, but rejected it as unable to provide the observed emission. There appear to be three contributing reasons for our difference: they compared the theory of a single shock viewed face on with their maximum observed surface brightness, $10^{-3} \text{ ergs cm}^{-2} \text{ s}^{-1} \text{ sr}^{-1}$, rather than an estimated average which for $10^3 L_\odot$ would be a factor of 10 lower; in addition, the average surface brightness of a spherical emitting surface is four times that of the local normal value for one side; and, finally, we have an additional factor of 2.5 to include the effects of current shell formation. The net effect is a factor of 100 which is just the difference between their estimate of the rate per unit area that the shock would have to be encountering ions and the $10^8 \text{ atoms cm}^{-2} \text{ s}^{-1}$ in our model. This caused them to believe that an unacceptably high ram pressure was somehow present where the [OI] emission occurred, and that that was somehow connected to an encounter with dense molecular material. In our model this is unnecessary: the correct total emission is found, and like the radio continuum and optical emission, there are local enhancements over the average of more than a factor of 10 due to rippling and edge brightening of the thin shell.

3.6 The Gamma Rays

It is fairly straightforward to estimate the maximum gamma ray intensity from cosmic ray ions interacting with the mass in the dense shell. Compression of the nonrelativistic component of ambient CR ions, or acceleration of ions in the remnant can potentially lead to a CR pressure in the shell comparable to the magnetic pressure, their sum being the shell pressure, approximately $2.8 \times 10^{-9} \text{ dyn cm}^{-2}$. This amounts to an enhancement of the ion pressure by a factor of 1400 over ambient. From the review by Bloemen (1989), and models in Esposito *et al.* (1996), we infer that this enhancement would lead to a gamma ray production rate above 100 MeV , from π^0 decay, of about $2.2 \times 10^{-22} \text{ photons s}^{-1}$ per H atom in the shell. For a shell mass of about $450 M_\odot$, as found in our 2d modeling later in the paper, and a distance of 2.5 kpc , the maximum flux would be $12 \times 10^{-8} \text{ photons cm}^{-2} \text{ s}^{-1}$, about a fourth of the observed value, concentrated in the east or northeast. (The total mass interior to W44, in our model, is about $1000 M_\odot$, but in our simplest picture we do not expect the more diffuse portions in the interior to be subjected to this high cosmic ray pressure. With some leakage and the associated additional compression, however, more of the remnant's mass may be exposed.) One may suppose that cosmic rays are leaking out of the remnant altogether, and irradiating the nearby dense molecular material, though if they do so at greatly reduced pressure, vastly more mass will be required for interaction. (Esposito *et al.*, 1996, found that irradiation of the entire Wooten cloud would require an average cosmic ray enhancement over ambient of a factor of about 80.)

If diffusion prevents the CR ion pressure from limiting the compression to the low value implied above (about 40), the bremsstrahlung component of the gamma rays can be enhanced by an similarly large factor. Generalizing on the methods of Section 3.4.1, the ratio of Gamma ray

bremsstrahlung to radio synchrotron enhancement factors turns out to be $x^{-\alpha_{\text{eff}}}$, where x is the compression factor and α_{eff} is the effective spectral index, which we have taken as 0.5. Comparison with our previous results for the van der Laan mechanism yields an overall gain of

$$G_{\gamma}(x) \approx 800(x/100)^{1.5}. \quad (24)$$

Again following the review by Bloemen (1989), and models in Esposito *et al.* (1996), we infer that this enhancement, for $x = 100$, would lead to a gamma ray production rate above 100 MeV of about 6×10^{-23} photons s^{-1} per H atom in the shell. For the shell mass and distance given above, the flux would be about 4×10^{-8} photons $\text{cm}^{-2} \text{s}^{-1}$, about 30% of the upper limit from π^0 decay and 7% of the observed gamma ray flux. Recalling from our discussion of the synchrotron radiation that the observed flux required approximately 4 times more CR electrons than anticipated from solar neighborhood estimates, and noting that electrons in the same energy range would be responsible for both the synchrotron and bremsstrahlung, we conclude that the gamma ray estimate must be raised by a similar factor, to 16×10^{-8} photons $\text{cm}^{-2} \text{s}^{-1}$, comparable to our upper limit from π^0 decay. Both mechanisms therefore require more target mass than our model provides, by about the same factor.

An alternative approach employed by deJager and Mastichiadis (1997), solves for the CR electron populations needed to produce both the synchrotron and bremsstrahlung. Taking the ratio, they obtain a relationship between the required magnetic field and density in the interaction region if both are to be produced. Interpreting the interaction region as the shell in our model, their result for the CR population required to produce the synchrotron is consistent with our previous conclusions. Their result for the required shell density for generation of the gamma rays can be summarized as $n_{\text{dJM}} \approx 25 \text{ cm}^{-3} (B/10\mu\text{G})^{1.33}$, while in our model we anticipate $n_{\text{shell}} \approx 20 \text{ cm}^{-3} (B/10\mu\text{G})$. At the shell fields of 180 to 260 μG of our model, the gamma ray production would require a shell density about 7 times that available. We repeated their analysis with a slightly steeper index and found the disparity to be slightly less, but still a factor of 4, consistent with our conclusion above that the electrons required in our shell to produce the synchrotron fail by about a factor of 4 to produce the observed gamma rays.

The contribution expected from inverse Compton radiation was also calculated by deJager and Mastichiadis, assuming a radiation field that is enhanced by the glowing dust in the neighboring molecular cloud. They concluded that the contribution was less than that from bremsstrahlung when the mean density in the interaction region exceeds about 10 cm^{-3} , a very low value compared to that found in our shell. Inverse Compton will also arise from CR electrons within the remnant but not yet swept into the dense shell, but that too appears negligible.

The net result of this investigation is that the dense shell in our model should produce gamma rays at roughly 25 to 50% of the rate actually observed in the vicinity by EGRET.

3.7 Evolution in a Density Gradient

Approximation to Kompaneets

In planning the use of a 2d hydrocode to provide a model including the partial shell formation of W44, we assumed the ambient density to have the exponential distribution:

$$\rho_{\text{o}}(z) = \rho_{*} e^{-z/h}, \quad (25)$$

where ρ_{*} is at the explosion site, and z is the distance from it, measured down the density gradient. Thus, to specify a model, the 1D input parameters (the explosion energy E_{o} and the ambient density ρ_{o}) have to be supplemented by the stratification scale-height h . The parameter space for initialization of a run is therefore three-dimensional, with age a fourth parameter. As high-resolution simulations in two dimensions are expensive, an extensive numerical survey of that space is not possible. Therefore, we searched for appropriate input parameters with the help of analytical calculations based on the Kompaneets Approximation (Kompaneets, 1960).

The basic idea of the Kompaneets Approximation is to assume that the post-shock pressure p_{s} is uniform over the surface of the remnant, while the evolution occurs in an exponentially stratified medium. For a strong non-radiative shock in a $\gamma = \frac{5}{3}$ gas, $p_{\text{s}} = \frac{3}{4}\rho_{\text{o}}v_{\text{s}}^2$, where v_{s} is the shock velocity and ρ_{o} is the ambient gas density. With uniform post-shock pressure, the local shock

speed is inversely proportional to the square root of the local ambient density. Thus the evolution of the shape of the remnant can be calculated without first knowing the time evolution. Once the shape is known, as a function of some size variable such as the semi-major axis, the volume can be calculated as well. Then, because the pressure is inversely proportional to the volume, the time can be found from an integration.

Maciejewski and Cox (1998) extend this approach in two ways, the first of which is to assume that the structure of the remnant is closely approximated by a prolate ellipsoid of semi major and minor axes a and b . They then readily find the semi-minor axis b , and the distance s by which the center of the ellipsoid has displaced from the explosion site, as functions of semi-major axis a . A surprising result of this exercise is that even remnants extending over several scale heights remain nearly spherical; the principal geometrical effect of the gradient is to shift the remnant center gradually away from the explosion site. (See also Dohm-Palmer and Jones, 1996, for a thorough discussion of this behavior based on 2d hydrodynamic modeling.)

Assuming the postshock pressure, explosion energy, and volume have the same relationship as in the 1D Sedov solution determines the dependence of the shell expansion velocity on the SNR volume, and an expression for the time derivative of the semi-major axis. Numerical integration then yields the time evolution $t(a)$, at which point, all of the quantities parameterized by the semi-major axis a can be expressed as functions of time.

Cooling and shell formation times

Maciejewski and Cox (1998) also evaluate the progression of the cooling time over a remnant in a density gradient, in almost exact parallel to the 1-d case. With the Kahn approximation, the incremental cooling time Δt_{cool} of a recently shocked parcel depends on the post shock pressure and the local preshock density. Adding that to the time at which a parcel is shocked determines its time to finish cooling. Minimizing t_{finish} over parcels (for a particular direction in the 2d case) determines the cooling time on that part of the remnant. Finally, multiplying by 7/6ths supplies an estimate of the time for shell formation. By performing this calculation for the remnant's dense end, tenuous end, and equator, the combination of Kahn and Kompaneets approximations provides a useful tool for the exploration of shell formation over the surface.

Even a modest density gradient leads to a great spread in cooling and shell formation times for different parts of the remnant's surface, making it possible to select input parameters which will lead to any desired degree of partial shell formation.

We examined a wide range of input parameters. In particular, we used our analytical method to generate plots on the ρ_*-h plane for assumed E_0 and linear size of the remnant. The plotted quantities included the time required to reach the assumed size, the post-shock pressure, the cooling and shell formation time-scales for the dense, equatorial, and tenuous directions, and the shock velocities in those directions. (Although the Kompaneets model, like the Sedov model, cannot be used very reliably to estimate quantities after shell formation has occurred, we make the usual approximation that shortly after shell formation the shell velocity is about 3/4ths of the shock velocity predicted for the non-radiative evolution.) In the limit of large scale heights, the results are consistent with our 1D calculations.

W44's parameters

In this way we were able to locate regions of parameter space which promised to satisfy the observational constraints discussed for the 1-d model, adding the further condition that shell formation must be well underway on the dense end, just commencing at the equator, and not yet present on the open more tenuous end. This must be reconciled with a substantial radial velocity for the receding part of the 21 cm shell.

These constraints turned out not to be sufficient to determine the scale height uniquely. In the end we chose to examine the most asymmetric (smallest scale-height) case that appeared to be viable; in it the cooling times on the high and low density ends differ considerably, but the expansion velocity into the densest medium is still large (models with still smaller scale-heights have too low an expansion velocity on the dense end). The selected input parameters and estimated characteristics of the remnant at 20,000 years are shown in Table 2 while Figure 1 summarizes the configuration and goal of the evolution.

Table 2: 2D Model Parameters and Predicted Characteristics

ρ_* (g cm ⁻³)	1.317×10^{-23}		
n_* (cm ⁻³)	6.2		
h (pc)	22		
E_o (ergs)	10^{51}		
time (yr)	dense end	equator	tenuous end
t_{cool}	12,000	17,000	25,500
t_{shell}	14,000	20,000	30,000
At 20,000 years:			
$a = 11.9$ pc, $p_C = 1.49 \times 10^{-9}$ dyn cm ⁻²			
speed (km s ⁻¹)	dense end	equator	tenuous end
shock	178	233	305
shell	133	175	NA

3.8 Sgro-Chevalier and Approximate Scalings

As it is unlikely that the hydrodynamic models will produce a remnant of precisely the size desired, it is useful to be aware of the Sgro-Chevalier scaling law (Sgro, 1972, Chevalier, 1974), that each evolution represents a family of evolutions with the same value of the parameter En_o^2 . This scaling was based on the fact that both ionization and cooling have temperature dependent two-body rates, and extends itself to include models with differing electron and ion temperatures, thermal conduction, and dust sputtering. In our case, for example, the hydrodynamic runs delivered models with radii of 11 pc, which would need to be placed at a distance of 2200 pc to have the correct angular size. The Sgro-Chevalier family member with a radius of 12.5 pc and distance of 2500 pc has the same temperature and velocity structure and the same distribution of ionization, but has an initial density of 5.5 cm^{-3} , an energy of $E_{51} = 1.3$, an age of 22,700 years, x-ray surface brightness and count rate (at the same angular size) reduced by a factor of 0.88, and unchanged synchrotron flux density. The shell mass is higher by the same factor as the energy, 1.3.

A more general but more approximate scaling, searching for a remnant at the same evolutionary stage as a specific hydrodynamic model but with a different radius, can be based on Equations 8, 22, and noticing that for collisional equilibrium plasmas with temperatures in the range 3 to 8×10^6 K, the ROSAT counts per emission measure function is approximately proportional to T^2 , particularly with significant absorption. The latter implies that the x-ray band luminosity is approximately proportional to $R^3 p^2$. The inferred scaling is that at a given evolutionary state, the various model parameters scale with n_o and En_o^2 as: $R_{\text{shock}} \propto n_o^{-1} (En_o^2)^{2/7}$, $t \propto n_o^{-1} (En_o^2)^{3/14}$, $v \propto (En_o^2)^{1/14}$, $T \propto (En_o^2)^{1/7}$, $S_{\text{x-Ray}} \propto n_o (En_o^2)^{4/7}$, $F_{\text{x-Ray}} \propto \theta^2 n_o (En_o^2)^{4/7}$, and $F_{\text{synch}} \propto \theta^2 (En_o^2)^{3/7}$, where S and F refer to surface brightness and flux, and θ to angular size. Thus, scaling a model from one with a radius of 11 pc to one with a radius of 12.5 pc and constant E_{51} requires an initial density of 4.6 cm^{-3} , and describes a remnant with an age of 23,700 years, x-ray surface brightness and count rate (at the same angular size) reduced by a factor of 0.53, and a synchrotron flux density lower by 0.77. The shell mass is higher by 1.09, and unlike the Sgro-Chevalier scaling, the velocities and temperatures are reduced by factors of 0.96 and 0.92 respectively. With the slightly lower temperature the ionization and therefore the details of the spectrum will be slightly different as well.

We will return to these results in discussing the hydrodynamic models. The main feature, however, is that all changes are moderate, essentially within uncertainties, except for the change in the X-ray surface brightness which is lowered significantly in the constant energy scaling.

3.9 Summary of the Analytical Section

According to our analytic approximations, an explosion of 10^{51} ergs into a medium with scale height of 22 pc and a density of approximately 6 cm^{-3} at the explosion site, when viewed at an age of 20,000 years has the following successes as a model of W44:

1. Its radius is consistent with the angular size and distance.
2. It will have formed a neutral hydrogen shell on one side (left rear with our orientation), with approximately the observed column density.
3. The expansion velocity of the HI shell will be close to that observed.
4. With thermal conduction at roughly its unquenched level, the central temperature and density are in agreement with those found from the x-ray emission. The dependence of the values on the actual magnitude of the conductivity is weak.
5. The temperature near the edge will be too low to contribute substantially to the x-ray emission, so that spectral softening with radius, particularly when combined with the high observed column density of intervening absorbers, can provide the appearance of center filled x-ray emission.
6. The van der Laan mechanism—synchrotron enhancement by compression of ambient cosmic ray electrons and magnetic field—can provide the observed radio continuum emission, but only with about a factor of 4 higher ambient CR electron population than estimated for the solar neighborhood. Additional complicating factors cannot be ruled out, and we discussed the possibility of diffusive acceleration boosting the energies of the ambient cosmic ray electrons in the gas subshock or further acceleration in the converging flows bounding the dense shell.
7. On-going shell formation and the radiative shock on the denser half lead to roughly 2000 L_{\odot} of high contrast filamentary $H\alpha$ from the dense fast moving shell, consistent with that measured after allowing for extinction, plus about 800 L_{\odot} of $H\alpha$ from diffuse fluorescence in the surrounding 3 pc or so of stationary ambient gas. The shell radiation is predicted to include also the full spectrum characteristic of a fast radiative shock, including amounts of [SII] and $63 \mu\text{m}$ [OI] emission completely consistent with those actually observed.
8. The gamma ray emission expected from the dense shell is 25 to 50% of that seen in the vicinity with EGRET.

4 Physics Assumptions, Justifications, and Implementations in the Hydrocodes

This section surveys the assumptions and methods of the hydrocodes employed in the next two sections to examine the spatial configuration of the remnant model’s characteristics, its appearances in 21 cm, radio synchrotron, and x-ray emission, and its x-ray spectrum. Particular attention is paid to justification of the inclusion of thermal conduction in the hot interior of the remnant.

4.1 Pressure

The thermal pressure is that of an ideal monoatomic gas with solar composition, assuming full ionization of hydrogen and helium, and equal temperatures for electrons and ions. Nonthermal pressure is represented via an isotropic term proportional to n^2 , whose principle effect is to limit the compression of the cold dense shell to a realistic value. Although this is referred to as magnetic pressure and the density dependence justified by flux freezing and compression of the tangential component, the codes do not perform magnetohydrodynamic calculations. Cosmic ray acceleration by the shock is assumed to have a negligible effect on the shock or remnant structure.

4.2 Thermal Radiation

In the 1-d code, nonequilibrium ionization and the corresponding cooling rates and spectra are followed in each parcel with the Raymond and Smith codes (Raymond and Smith 1977, Raymond 1995), accelerated with modifications using tables of rate coefficients provided by Edgar (1994).

The abundance set adopted was that of Grevesse and Anders (1988). Radiative transfer between parcels was not included.

Because the 2d code does not follow the ion states with time, it is necessary to estimate the radiation rate with a cooling function. As proposed by Edgar (Edgar and Chevalier, 1986), a pseudo non-equilibrium radiative cooling table was adopted. It contains the non-equilibrium radiative cooling coefficient versus temperature for an optically thin plasma that was shock heated to 10^8 K (though the choice of upper temperature has little effect) and then isobarically cooled.

The model x-ray spectra were also generated with the Raymond and Smith code, based on the temperature and non-equilibrium ionization state of each parcel previously calculated by the 1-d hydrocode. The spectrum was attenuated using the absorption curves of Morrison & McCammon (1983), and then convolved with the ROSAT PSPC and Einstein SSS response functions.

4.3 Dust

For the most part, dust is assumed to be non-existent within the hot portions of the remnant. As shown by Smith *et al.* (1996), this assumption has little effect on the inferred cooling timescale of the gas parcels. The elemental abundances do, however, affect the spectrum. As a result, we discuss the results of a 1-d run with dust destruction included explicitly, using the rate model of Smith *et al.* (1996).

4.4 Thermal Conduction

The thermal conduction treatment is similar to that of Slavin and Cox (1992), a single temperature model with an electron thermal conductivity which is classical in regions of weak temperature gradient but bounded by the saturation limit when the gradient is large. As shown in Cui and Cox (1992), by the times of interest here this provides a description which is close to that of models with different electron and ion temperatures and their corresponding electron and ion conductivities.

In the present study, however, a single temperature model is not without dangers: examination of the Cui and Cox thermal structures shows that there is disparity at the center of the remnant. In their case 4, in which the electron and ion temperatures are followed separately with only coulomb collisions to equilibrate them but each with its own conductivity, there is a persistent core of hotter ions and lower density (about a factor of 3 in the inner third in radius), compared to the single temperature case. Normally, this disparity is unimportant; we do not generally imagine these hydrocode models to be useful in the central parts of the remnant where the structure is surely affected by the details of the explosion and the pre-supernova stellar evolution. In Cui and Cox, for example, it is probably a relic of initializing with a Sedov structure. But, when we are purporting to model the central x-ray emission, we cannot help being concerned about this point.

The next concern derives from the considerable uncertainty regarding how much conduction actually occurs in the hot interior of an SNR, relative to standard formulae, and how the answer depends on time. Although we regard this as a sufficiently difficult problem that observations of objects like W44 will probably be called upon to solve it, there are some points worth making. For example, it is important to realize that a very small amount of transport, compared to the classical heat flux, will make a very large difference to the central structure of a remnant (section 3.3), even if that transport is active only when the remnant is rather young.

The most common arguments against the presence of significant heat transport in remnants have to do with the strong suppression of conductivity transverse to magnetic fields. In 2d MHD models, a uniform ambient field is distorted outward in the bubble, in most places providing a significant tangential component, guiding what conduction there is to the magnetic caps. Arguing that there has been considerable turbulence in the center, or that the field was largely irregular in the first place, encourages the idea that all conduction paths along the field will be very long, suppressing conduction to a large degree.

Of course, the self-same turbulence that was imagined to have tangled the field would also have intermixed the entropy components, accomplishing largely the same purpose as conduction. At the very least, it would have smeared a tangled mixture of different temperature components across the interior structure. In addition, field line wandering (Jokipii and Parker, 1969) then allows transport among seemingly isolated regions.

In very young remnants, still interacting with their own wind material, there is a lot of radial mixing and the dominant field component is radial. This would seem not to suppress conduction substantially. On the other hand, for W44, entropy mixing among roughly the innermost 30-100 M_{\odot} is needed.

In point of fact, all conceptions of thermal conduction in this environment are vastly too simplistic: the collision mean free paths are very long; the stellar ejecta are surely an important complication; nonlaminar flow with mixing and turbulence has almost surely occurred; and the strict adiabaticity of the Sedov solution is surely the worst possible approximation. Our use of classical conductivity may seem naive, but, when safeguarded for saturation, it provides a reasonable, physically based estimate for the rate of transport. It could, in fact be an underestimate if turbulent diffusion is important in remnant interiors.

Two papers which have discussed magnetic suppression of conduction and limits on that suppression include Rosner and Tucker (1989), and Tao (1995).

In summary, no existing model offers a better idea. This one is important to explore, but such exploration must be followed by careful discussion of the discrepancies so we can have some indication of what other processes might be important.

Transport of ions

A related issue is that in remnant interiors the transport of energy is very likely accompanied by the convection or diffusion of elemental abundances and of the ionization structure. This too could alter the x-ray spectrum and surface brightness of the center, presumably moving toward greater uniformity.

Implementation of conduction

In the 2d hydrocode, expressions for the classical conductivity, the saturation flux, and the interpolation between them were taken from Slavin and Cox (1992). The conduction equation is solved at the beginning of each base-grid time step on a uniform grid with the resolution corresponding to the resolution of the finest grid used in the simulation. An implicit, fractional-steps method of Yanenko (1971) is applied. The implementation is similar in 1d, except that the originally proposed formula for interpolation between classical and saturated fluxes ($F_{\text{total}} = F_{\text{class}}/[1 + |F_{\text{class}}|/F_{\text{sat}}]$) of Cowie and McKee (1977) was used. Except as noted, the classical conductivity assumed was the full unquenched value as given in §3.3.

4.5 Synchrotron Emissivity for Use With Hydrocode Results

Estimation via the methods of Section 3.4.1 of the radio synchrotron emission expected due to the van der Laan mechanism requires somewhat unusual accounting, evaluating for each parcel in the model its initial volume, compression factor, and gain. The specifics are: the emissivity of the ambient medium at 100 MHz was taken as 10^{-40} W/(m² Hz sr); the compression factor was taken as $x = \rho/\rho_0$ (where ρ_0 is the initial density of the parcel); the ambient emissivity was multiplied by the initial volume of the parcel, taken to be M/ρ_0 , dividing by 10^6 to accommodate the mixed units; that initial emission rate was multiplied by the gain at a given frequency, $G(x) \approx (\pi/4)x^2$ for an effective spectral index of 0.5, and then 4π to eliminate steradians. The final result is the parcel's spectral emission (in Watts Hz⁻¹).

To obtain the total spectral luminosity, the emission is summed over the parcels in the remnant. To turn this into a contribution to the observed flux density, it is divided by $4\pi d^2$ with the distance d in meters, to get Watts (m² Hz)⁻¹, and divided by 10^{-26} to convert to Janskys.

5 Two-Dimensional Model

5.1 Background

Purpose

The 2d modeling provides a fascinating look at the structure of the remnant as well as quantitative representations of the HI distribution, across the remnant and in radial velocity, and of the radio continuum emission distribution anticipated from the van der Laan mechanism. It also allows us to examine the x-ray emission from the distribution of density and temperature in the

interior to see whether lack of sphericity might invalidate our more detailed 1d model of the x-ray surface brightness distribution and spectrum.

Code Description

The hydrodynamic and thermal conduction equations are solved with the help of the AMRA code (Plewa & Müller 1998), which combines the AMR (adaptive mesh refinement) algorithm of Berger and Colella (1989) and the PPM method of Colella & Woodward (1984). It has also been recently used in a numerical study of the evolution of ejecta fragments by Cid-Fernandes *et al.* (1996). The specifics of our implementation of thermal conduction, nonthermal pressure, and thermal radiation are discussed in section 4. (The effective magnetic field strength assumed was quite low, corresponding to $2.1 \mu\text{G}$ at 20 cm^{-3} and proportional to density, so the nonthermal pressure was felt only in the dense shell and not very strongly even there.)

The present application employs spherical coordinates (r, θ, ϕ) and rotational symmetry with respect to the polar $(\theta = 0, 180^\circ)$ axis. The initial grid extends over radii $0.0 \leq r \leq r_{\text{max}}$ and polar angles $0^\circ \leq \theta \leq 180^\circ$, containing 128 and 15 uniformly distributed points in r and θ , respectively. The adaptive mesh refinement takes place in two stages, as needed, with total factors of up to 20 and 6 improvement in r and θ resolution. Thus, the resolution of the finest grid is equivalent to that of a uniform grid of 2560×90 points extending over the whole computational domain, while requiring about a factor of 15 less CPU time. This resolution was chosen after 1d experiments showed that with 2560 zones in radius the fully formed shell will be resolved into not less than 10 cells. At lower resolution we would not have been able to describe the velocity distribution of the cold material. Even with the adaptive mesh, the CPU time used for the simulation presented below amounts to ~ 10 days of the CRAY J90.

Initial conditions

The code is initialized at a remnant age of 300 years, with the explosion energy in expansion of the ejecta. The mass of the ejecta is $5 M_\odot$; the density and velocity profiles are those used by Cid-Fernandes *et al.* (1996). The outer expansion velocity is about 5000 km s^{-1} and therefore the radius of the ejecta at initialization is about 1.5 pc.

The values assumed for the explosion energy (10^{51} ergs), ambient density at the explosion site (6.2 cm^{-3}), and scale height of the ambient density distribution (22 pc) are those found from our analytical study as recorded in Table 2.

5.2 Results

Each cell, or parcel, consists of an annulus in ϕ , with volume $2\pi r^2 \sin \theta \delta r \delta \theta$. At a specific evolutionary time the output for each annulus consists of the average r and θ , along with the corresponding density, temperature, mass, and the two components of velocity. From these, the thermal and magnetic pressures can be inferred, along with the x-ray emission (assuming collisional equilibrium) and radio continuum emissivities.

5.2.1 Structure

Figures 2, 3, and 4 show the density, temperature, and pressure structures of the simulated remnant at an age of 20,000 years. In the transparent side view of Fig 2, the densities in all cells are shown, versus their locations along the major axis. The locus of values, between 3 and 10 cm^{-3} , making up the straight diagonal line extending beyond the remnant shows the exponential density distribution of the ambient medium. The diameter (major axis) is seen to be just over 22 pc, essentially one scale height in the ambient medium.

There are deviations from spherical symmetry in the low density interior, but they are quite modest. The central density is about 15% of ambient at the equator, its minimum being about 1.0 cm^{-3} , as predicted by the analytical modeling. In addition the distribution is very flat, exceeding the minimum by less than a factor of two over a large region in the interior.

The cells with very high density are those in the cold dense shell. As we discuss below, the thermal pressure was too large at high density in this run, and the magnetic pressure was too low. With these conditions, the densest ones should have been compressed by about a factor of 120 over ambient, and are, as shown. Complete shell formation, shown by the locus of highest density cells,

has reached from the dense end to the equator, just as predicted, beyond which the maximum compression fades sharply.

The many cells with compressions somewhat less than maximum show the well resolved transition of material which has begun cooling but has not yet reached its limiting density. At the tenuous end, shock compression by only the adiabatic factor of 4 is apparent, while not far away where radiation is just beginning to affect the structure, that factor of 4 is followed by further compression. The final distribution of grid resolution is also apparent in the figure, where the regions of highest density have the greatest concentration of cells in r and θ .

The temperature structure in Figure 3 is shown as a 3d surface plot with the densest end on the near left side. It shows a central temperature of about 6×10^6 K, consistent with our expectation from the conduction analysis (Section 3.3), with a slightly lower shoulder just left of center where the density was higher. The trough in temperature behind the shock on the tenuous end is a surprise, indicating that the shock there is already becoming radiative where our analysis had predicted a cooling time of 25,500 years (Table 2). This is consistent, however, with indications (below) of a relatively low pressure on the tenuous end. As discussed in Maciejewski and Cox (1998), a pressure difference between the two ends is apparently also responsible for the reduced displacement observed for the remnant center. Apart from the aforementioned shoulder and the radiative shock girding the tenuous end, the temperature structure is nearly symmetric and parabolic. Both the central value and the general distribution are quite similar to 1d results presented in Section 6 below.

The pressure in the interior of the remnant (Figure 4) is very flat in the center with a value of 1.6×10^{-9} dyn cm $^{-2}$, but drops abruptly by 5% about halfway to the edge. On the tenuous end, this drop leads to a broad shallow valley at 85% of the central pressure. On the dense end the pressure continues to drop with increasing slope, to a deep trough.

Very close to the edge on the dense end, it is apparent that the low pressure is due to rapid radiative cooling. The structure further in, which can also be discerned in the density details of Figure 2, resembles a substantial rarefaction moving inward or a compressional wave moving outward. Such waves are fairly commonly found in hydrodynamic models although none is obvious in the particular 1d model presented in the next section. When present, they have very long reverberation periods and thus appear for a long time as nearly stable features. We explored several possible sources for this structure in our 2d run and found that the high flat central pressure, its weak but abrupt edge, and its asphericity are the residual of the reflected reverse shock. (An experimental 1d run with the same initialization as the 2d run produced a very similar structure.) Because a reverse shock is required to raise the pressure of the center, and it will surely be reflected to some degree, there should be a substantial time during which this sort of structure is present within a remnant. But detailed conclusions based on its presence in a particular remnant model should be regarded with some suspicion. When it is found, where, and with what strength, depends on the initialization. Perhaps a fruitful approach would be to search the x-ray emission pattern of a remnant for indications of such a structure and, if found, to use the structure to evaluate models of the remnant's early state.

Stating our pressure results more optimistically, the interior pressures in our standard 1d and 2d runs differ by less than 30% anywhere that the temperature exceeds 2×10^6 K. The differences will have negligible impact on the interpretation of the x-ray data.

The pressure structure at the very edge of the remnant bears an imprint of both the cooling history and the way we treat cooling in 2d. (Note that the pressure spikes shown are an artifact of the way in which the figure was prepared, not a characteristic of the model. They are due to incomplete sampling of the densest region in converting the model data from spherical to cartesian coordinates for the plot. This makes the shell conveniently transparent, but inaccurately suggests that it was poorly resolved in the model.) At the tenuous end, the pressure maximum is in the immediate post shock gas, prior to the onset of cooling. Further inward where cooling has begun, the pressure drops precipitously. The structure at this end is entirely resolved. At the high density end, the radiative shock is unresolved and the high pressure region is in the already cold dense shell, itself trailed by a deep pressure trough of cold but not yet compressed material. Comparing the maximum pressures at the two ends, we found 3.4×10^{-9} and 2.4×10^{-9} dyn cm $^{-2}$, for the dense and tenuous ends, respectively. Moving away from either end the edge pressure drops rather rapidly. On the tenuous end this appears to be due to the onset of cooling, which coupled with the

inverse temperature dependence of the cooling coefficient, temporarily stalls the shock, possibly leading to a period of instability and secondary shock formation (Falle, 1975, 1981). This is most exaggerated in an extended region of the remnant's surface over which the post shock pressure seems to be very low, just toward the tenuous end from the equator. In this region the radiative shock appears not to be resolved (the initial compression exceeds 4), but cooling is so rapid that the post shock pressure is small and the shock velocity temporarily low. On the dense half, the pressure in the cold shell drops a factor of two between the end and the equator. On the whole, these peculiarities in the pressure structure provide the biggest deviations from the expectations based on analytic and 1d models.

In summary, the magnitudes of central density, temperature and pressure are all as expected. Similarly, shell formation over half the surface has occurred as planned. There were some new but qualitatively understandable features brought to light, particularly the strong variation of edge pressure over the surface at this epoch, and the seemingly premature onset of cooling on the tenuous end. We are left not knowing whether the detailed interior pressure distribution of the 2d case is a better or worse approximation than the 1d structure presented in Section 6.2.1, but are relieved that the differences are modest.

5.2.2 HI Shell

In the particular orientation of our 2d model, the symmetry axis is tilted 40 degrees from the line of sight with the dense end on the far side, and toward the northeast, giving us a glancing view into the open end of the half shell. With this projection, most of its dense material (and associated strong magnetic field) is in the northeast, where the average radio continuum brightness is highest, and the dense gas is moving predominately away, so that the ranges of expansion velocities observable via 21 centimeter emission are occupied only on the receding side, as observed.

In preparing the figures of this section, the mass of each r, θ annulus of the calculation is represented by a proportional number of dots, randomly distributed within the annular volume. The spatial coordinates and velocity components of each dot are then tracked through the rotations to the final projection. (In later sections on the radio continuum and x-ray appearances, the process is similar but the number of dots per annulus is chosen in proportion to emission rather than mass.) The dot density in the shading thus represents the projected surface density (or surface brightness in the emission pictures). Unless otherwise noted, the assumed distance of W44 was that required to give an angular diameter of $35'$, about 2200 pc, closer even than our revised distance estimate as quoted in Table 1. Methods for scaling the results were presented in Section 3.8 and their application will be discussed further in the conclusions.

Figures 5 and 6 present our results for the distributions of mass and velocity in the dense shell, in formats for direct comparison with the observations of Koo and Heiles (1995). They include only cold material more dense than 100 cm^{-3} , assuring a sufficiently short (~ 1000 year) recombination time to achieve neutrality (the ionization state not actually having been tracked in the model).

Figure 5 consists of 4 panels, two of which are projected column density, the others being position velocity diagrams. The upper right panel shows the total column density map of the dense half shell. As expected, it is concentrated toward the northeast, sharply bounded and edge brightened there, but fades out gradually to the southwest.

This view, however, is not available to observers because of the large amount of low velocity hydrogen toward W44. The corresponding view presented by Koo and Heiles (1995) is limited to the velocity range $v_{\text{LSR}} = 135$ to 170 km s^{-1} and displayed as their Figure 1a. Their figure and the corresponding model column density map for that velocity range (including the systemic velocity of $+43 \text{ km s}^{-1}$) are shown in the lower left (oblique view) panel of Figure 5. The model view changes considerably when limited to this velocity range. It is much more diffuse, lacking the sharp bright northeastern edge, smaller, more symmetric, and has a hole in the center from omission of highest velocities. With these changes, it bears a very strong resemblance to the HI observations.

The model's restricted velocity view has a total diameter of about $25'$ (a mass weighted diameter of about $18'$) versus the shell's total diameter of about $35'$. For comparison, Koo and Heiles quote the mass weighted radius at $v_{\text{LSR}} = 140 \text{ km s}^{-1}$ as $7.5'$. The corresponding mass weighted $15'$ diameter is smaller than our model. As will become apparent below, the model is in good agreement with the data envelope in position velocity diagrams, but the HI data are more filled in velocity

space, leading to a lower mass weighted size.

Taking model data from within the apertures outlined in the upper right panel of Figure 5, the upper left and lower right panels show the corresponding position velocity diagrams. In contrast to the total surface density plots, the half shell of the model is immediately apparent. The model remnant would be observable in 21 cm almost exclusively on the rear (receding) surface, as is W44. (If our model were absolutely correct in its degree of shell formation and orientation, however, we would predict the observability of a small quantity of rapidly approaching HI in the northeast.)

In Figure 6, portions of the position velocity diagrams with W44's systemic velocity of +43 km/s added, are replotted with the same restricted velocity range as in Figs. 1c and 1d of Koo & Heiles (1995). In addition, the HI data were kindly supplied to us by Koo, and are shown for comparison.

The correspondence between the observations and the model is again very good: both show the highest velocity of the bulk of the material to be about 180 km/s, but with some moving as rapidly as 200 km/s. The highest velocities are found toward the center, with lower values near the edge and a more hollow center, indicative of an expanding shell. The radial scales correspond very well on the whole, with the model distribution outlining the data and having a diameter of about 25' at 140 km s⁻¹, about 2/3rds of the actual remnant diameter.

As noted above, the observations seem to have a wider range of velocity at a given radius than does the model, with a lumpier distribution of material. The model is highly idealized, neglecting small scale irregularities in the ambient medium and any turbulence that may be present. As we discuss and demonstrate below, the radio continuum maps show strong filamentation that is associated with surface irregularities which, in addition to their effect on the surface brightness profile, will tend to broaden and disturb the velocity structure. For example, a bright radio continuum filament indicates a tangential view of that portion of the remnant surface. When such a filament is seen projected well away from the remnant edge, the line of sight velocity there will be very small, because the surface motion is turned crossways. Any remnant whose radio continuum map shows an intricately textured surface like that of W44 will have a much broader and more disturbed radial velocity distribution in 21 cm than any smooth shell model.

Considering that the model made no attempt to include any irregularities, it is somewhat surprising that its velocity width at the remnant center is as broad as it is. This appears to be due to the ongoing rapid development of the shell. There is material which has cooled and been compressed, but has not yet merged with the densest gas in velocity space. This is indicative of the strong velocity convergence in the neighborhood of the densest regions, as discussed in Section 3.4.2 with regard to suppression of cosmic ray diffusion from the shell. There may also be a contribution from the instability of radiative shock waves at high velocity (Falle, 1975, 1981).

Koo and Heiles (1995) reported that the mass associated with the shell and having $v_{\text{LSR}} \geq 130$ km s⁻¹ is $73 \pm 3 M_{\odot}$. The mass of the simulated shell having velocities within this range is 149 M_{\odot} at an age of 20,000 years. The dependence of the model results on remnant age are shown in Table 3, both for the mass within that velocity range and for the total mass at density above 100 cm⁻³. (The results depend only slightly on the density criterion for inclusion in the neutral shell.) Apparently the model shell's cold mass is about a factor of two larger than the observed HI mass, a conclusion that does not depend strongly on the age at which it is evaluated.

Several neglected factors are probably responsible for this differential. For example, the shell is partly ionized. In Section 3.5 we found that (because of photoionization) each atom joining the shell had to recombine about 3 times. We expect the ionized gas in the shell to be roughly equal to that collected during the past 3000 years (3 recombination times at 100 cm⁻³), lowering our estimate of the neutral mass with $v_{\text{LSR}} \geq 130$ km s⁻¹ by up to 50 M_{\odot} . Similarly, the presence of the OH masers implies that the shell is at least partly molecular. If 200 of the 450 M_{\odot} in the shell were H₂, there would be no discrepancy. Finally, the fact that the observed remnant has surface structure that broadens the velocity distribution in its position velocity diagrams makes it difficult to compare the amounts of mass in an observed velocity range. The distortion could easily have skewed the velocity distribution downward near the cutoff velocity, reducing the measured shell mass.

Table 3: Time Dependence of 2D Model Characteristics

Age (years)	16,000	17,000	19,000	20,000	21,000
Cooled Mass (M_{\odot})	230	310	475	565	655
Mass in Shell with $n \geq 100/\text{cc}$ (M_{\odot})	135	210	370	450	535
Shell Mass with $V(\text{LSR}) \geq 130 \text{ km/s}$ (M_{\odot})	60	88	134	149	157
Radio Continuum 100 MHz (Janskys)	104	179	346	423	503
ROSAT Hard Band (counts/s)					
NH = 1.0E22	8.5	7.3	5.5	4.8	4.2
NH = 1.5E22	4.8	4.1	3.1	2.7	2.4
NH = 2.0E22	2.9	2.5	1.9	1.6	1.4
ROSAT Soft Band (counts/s)					
NH = 1.0E22	29.0	24.9	18.9	16.6	14.7
NH = 1.5E22	7.5	6.5	4.9	4.3	3.8
NH = 2.0E22	2.5	2.1	1.6	1.4	1.2

5.2.3 Radio Continuum

This section discusses the radio continuum emission expected due to the van der Laan mechanism, following the prescription in Section 4.5. Before doing so, however, we had to overcome one difficulty. Our 2d model assumed an unrealistically low value for the magnetic pressure. In addition, cooling was suppressed below 10^4 K, yielding an excessive thermal pressure. Together these led to results for density in the shell that were unreliable (though the two effects roughly cancelled and the density structure turned out to be reasonable. For this section, we corrected the compression factor in each annulus of the calculation, under the assumptions that: the hydrocode provides a correct value for the annulus's total pressure, the initial density is the ambient density just outside the shell at the same z (that is, that material in the dense shell has not moved far in z), the ambient tangential field outside the remnant is $3\mu\text{G}$ independent of external density, and that thermal and cosmic ray pressures are negligible within the shell (yielding a reasonable but optimistic assessment). Setting the magnetic pressure equal to the total computed pressure in the annulus determines the corrected compression factor for calculating the gain. Following the rest of the prescription provided the flux densities shown in Table 3. As found in the analytic section, this slightly optimistic estimate of the van der Laan flux density is consistent with the observation of 500 Janskys at 100 MHz. But once again there is the hidden assumption that the background can be produced by CR electrons in the mean ambient field, an assumption that fails by approximately a factor of 4 when applied to estimates in the solar neighborhood.

The 2d model also makes possible a projected image of the synchrotron emission, prepared in much the same way as was done for the HI structure. Under the assumption that the true radio continuum emissivity is proportional to our van der Laan modeling, and neglecting the directionality and polarization of the emission relative to the magnetic field, our map for the radio continuum is shown for our standard projection in the upper right panel of Figure 7. A similar image in the lower left panel shows the view that would be had from a direction perpendicular to the major axis; the half shell of the model is obvious. The figure also shows three horizontal and three vertical slices through the emission. The central slices quantify the strong degree of edge brightening apparent on the northeast.

The observed radio continuum distribution, illustrated beautifully in Smith *et al.* (1993) and in Giacani *et al.* (1997), is qualitatively similar but differs in two significant characteristics. The observations in fact were the stimulus for our projected half shell model, giving the distinct impression of a view into an open hemisphere, brighter in the northeast than southwest because of the double contribution from the two sides in projection. Our model, however, has a blurred edge extending

further around the shell, and thus projects into a more rounded configuration with less of a step in overall brightness. The second major difference is that the observations show quite pronounced filamentation, some of which appears to be associated with the sharpness of the equatorial edge. Hester (1987) has shown in the case of the optical emission of radiative shocks that a high degree of filamentation can derive from spatial irregularities in very thin emitting structure. In order to test this as a possible source for the filamentation of the radio continuum in W44, we prepared an image of the 2d model in which the individual emission elements were radially displaced in a sinusoidal pattern resembling the corrugated surface of an acorn squash. The results are shown in Figure 8 and very clearly show that a modest degree of surface crinkling can lead to striking filamentation. The horizontal and vertical slices show the filamentation contrast.

In modeling the filamentation in this way, the areas of especially bright radio continuum are assumed to derive from tangencies along the surface from regions which are extremely thin. As such, they should also be filaments in HI, optical, and all other emissions associated with the dense shell and radiative shock, as is observed.

Because the ambient cosmic ray electrons have a flatter energy distribution at lower energies, the radio continuum spectrum of W44's filaments should be flatter than that of the remnant's more diffuse component. This comes about because, qualitatively, there are two layers of radio emission, a very thin bright one from fully compressed material in the dense shell, and a somewhat thicker layer from cooled material in the process of compression. The thinner layer dominates the filaments because it is most edge brightened by tangency, while the two layers contribute more equally to the diffuse component. On average, then, the filaments have suffered greater compression and their emission derives from electrons which were initially at lower energy, where the spectrum is flatter. Potential applications of this phenomena include the possibility of inferring the very low energy interstellar cosmic ray electron energy distribution from filament spectra of very high pressure (small, high density) supernova remnants.

5.2.4 X-Rays

The x-ray surface brightness distribution and count rate for the 2d model were calculated from equilibrium Raymond and Smith spectra, folded through ROSAT PSPC response functions for two bands (soft R4+R5+R6, 0.4 - 1.56 keV, and hard R7, 1.05- 2.04 keV), and attenuated by photoelectric absorption by the foreground material. The total count rates for both bands, at three absorption column densities, for five ages are shown in Table 3. The observed band ratio of about 1 for these two bands (Rho *et al.*, 1994) points to an absorption column between 1.8 and 1.9 $\times 10^{22}$ cm⁻². At an age of 20,000 years, the corresponding total predicted ROSAT PSPC count rate is then also close to the observed 4.2 s⁻¹ found by Harrus *et al.* (1997).

The distribution of X-ray surface brightness for this case is shown in Figure 9. It is brightest in the center, approximately gaussian in appearance, and highly symmetric about the center. The full width at half intensity is about 19', just over half the full diameter. There is nothing about the structure that appears to be particular to the two dimensionality of the calculation or lead one to suspect there was a significant density gradient in the ambient medium. The center of the emission is shifted slightly away from the explosions site, but is well centered within the remnant. Of course, when comparing with the observations, one has to bear in mind the strong sensitivity of the count rates to the absorption column density. It is quite possible that variability in the absorption screen leads to artificial structure in the observed x-ray surface brightness. Scattering of the X-rays by intervening dust may also be a factor.

The appearance the model remnant would have without absorption is shown in Figure 10. From this result, it is clear that at this particular age, the outer parts are everywhere too cool to contribute to the emission and the absence of the outer shell emission is not primarily due to absorption. The fact that the pressure drops somewhat away from the remnant center also contributes to this behavior.

From these results we are confident that 1D modeling of the nonequilibrium ionization structure and x-ray spectrum presented in the next section reasonably corresponds to a hypothetical 2d model which followed the ionization.

Table 4: Parameters of 1d Runs

$n_o = 6.2 \text{ atoms cm}^{-3}$, $E_o = 1.0 \times 10^{51} \text{ ergs}$, $t = 20,000 \text{ years}$			
Model	Conductivity	Dust Destruction	Abundances
A	full	utter	solar
B	zero	utter	solar
C	full	utter	enhanced
D	zero	utter	enhanced
E	1/10th	utter	solar
F	full	sputtering	solar

6 One-Dimensional Model

6.1 Background

Purpose

A variety of 1d hydrocode models were made during the course of this investigation. They were used to verify the approximate cooling time formula, to explore the lag time between cooling and shell formation described in Section 3.2, to explore the time development of shell mass and radio continuum emission, to measure the resolution needed in the 2d model, to examine the dependence of the central conditions (density and temperature) on the assumed degree of suppression of the conductivity, to explore the degree of dust destruction expected within the hot interior of the remnant, to simulate inclusion of additional heavy element abundances in the ejecta, to explore the dependence of the interior pressure structure on the SNR initialization characteristics as per Section 5.2.1, and to calculate non-equilibrium x-ray spectra for comparison with the surface brightness distribution and with the available spectral information.

Code Description

Our code architecture employs a Lagrangian mesh, based on the scheme discussed in Richtmyer and Morton (1967) and described in detail in Smith and Cox (1998). The method is similar to that of Cui and Cox (1992) and Slavin and Cox (1992). The ionization and emission characteristics are discussed in Section 4.

Initial conditions

A simulated supernova explosion is initialized as a 2 pc radius sphere containing 2 solar masses of ejecta with a velocity linearly proportional to the distance from the center.

The values assumed for the explosion energy (10^{51} ergs), and ambient density at the explosion site (6.2 cm^{-3}) are those found in our analytical survey and recorded in Table 2. All results reported are for an age of 20,000 years. With these parameters and age, the model SNR is found in an adolescent stage of shell formation. It approximates edge conditions only near the equator of the 2d model, and is therefore not directly useful in studying the radio continuum or shell development. We have, however, examined these characteristics at later times and in models that were higher in density to verify behaviors of the 2d results.

Results of six models appear below, differing in assumptions about the level of thermal conductivity (full, reduced, zero), dust destruction (utter, thermal spallation only) and abundances in the ejecta (solar, 5 solar). Their different characteristics are summarized in Table 4.

6.2 Results

At a specific evolutionary time the output for each parcel consists of the inner and outer radii and velocities of each parcel, plus averages of density, temperature, thermal and nonthermal pressures, and nonequilibrium ionization. In models following gradual dust destruction, or enrichment in ejecta, the gas phase elemental abundances are also recorded for each parcel. From these, the x-ray spectral emissivity of the hot interior, shell mass and its velocity distribution, and radio continuum emission can be calculated as described in Sections 4.2 and 4.5.

6.2.1 Structure

Figures 11, 12, and 13 show the density, temperature, and thermal pressure structures of Models A and B at an age of 20,000 years. The differences, due entirely to thermal conduction, are immediately apparent.¹ In agreement with the 2d run, the radius is just over 11 pc and the interior electron density in Model A is about 0.92 cm^{-3} (nuclear density about 0.84 cm^{-3}), and very flat. This central density is 13% of the ambient density, just as predicted in Section 3.3. For Model E (not shown), with its thermal conductivity reduced by a factor of 10, the central electron density is still fairly flat but has a value of only 0.51 cm^{-3} . The central density reduction by a factor of 1.8 with a conductivity reduction of 10 is also exactly that expected from the analytical work in Section 3.3.

The temperature structure in the interior of Model A also reconfirms the 2d model, dropping only gradually with radius from a central value of $6 \times 10^6 \text{ K}$, in the range consistent with x-ray observations. In the outer parts, thermal conduction has delayed the progress of shell formation somewhat and provided a slightly larger remnant. Models A and B both have similar temperature and density ranges in the outer parts, so that, as in Harrus *et al.* (1997), it is possible to find an x-ray model with a similar total luminosity, but it will be flatter or even shell like in surface brightness, and may exhibit a stronger radial temperature profile.

The pressure in the remnant interior is very flat in either case, as expected, with a value of about $1.5 \times 10^{-9} \text{ dyn cm}^{-2}$ for Model A. As previously mentioned in Section 5.2.1 the pressure distribution of Model A is smoother than that of the 2d model and the difference was traced to the different initializations.

6.2.2 X-ray Surface Brightness Distribution

Figures 14a and b compare the predicted radial flux distributions from Models A and B (after absorption) with observations in the ROSAT PSPC soft (R4+R5+R6, 0.4 - 1.56 keV) and hard (R7, 1.05- 2.04 keV) bands. The model spectra were attenuated by a constant $N_{\text{H}} = 1.89 \times 10^{22} \text{ cm}^{-2}$ (found by fitting the Model A spectra to observations, below), although Rho *et al.* (1994) found best fit values for collisional equilibrium isothermal models varying between 1.57 and $2.10 \times 10^{22} \text{ cm}^{-2}$ across the remnant. The model remnant was taken to be at a distance of 2.2 kpc for these plots so that the angular diameter of the shock would be $35'$. This has no effect on the magnitude of the surface brightness but determines the angular scale and PSPC count rate.

Obtaining a meaningful radial distribution from the asymmetric ROSAT image involved several steps. The data were cleaned and calibrated using the method described in Snowden *et al.* (1994), and following the examples given in Snowden (1994). Emission from a bright G star on the left side of image was then removed and, using Jones *et al.*'s (1993) choice for the nominal center ($\alpha, \delta = 18^{\text{h}}53^{\text{m}}30^{\text{s}}, 1^{\circ}15'$ (1950)) the data were averaged over a 90° angle in each of the four cardinal directions (north, south, east, west). The persistence in Figures 14a and b of the surface brightness to greater radii in the north is real: the X-ray distribution is longer north-south than east-west and the point chosen for the nominal center is south of its centroid.

Overall, the count rate and surface brightness distributions of Model A and our 2d model are in excellent agreement. Compared to observations, they account for several key features: the surface brightness is highest at the center, the limb is not brightened, and the total count rate of Model A is just 12% higher than observed (see Table 5). Model B, however, without conduction, has a factor of 2 too little emission overall and is edge brightened. (A model similar to B, by Harrus *et al.* (1997) was somewhat more successful.) The only apparent failings of the conductive models are that their emission distribution is dome-like while the observations resemble a peaked volcanic cone,² and that the 2d model is too symmetric, not providing the north—south elongation apparent in the image. The next few paragraphs record various experiments which explored model complications that might sharpen the central peak of the distribution.

Emission from Thermalized Ejecta?

¹ The glitches at a radius of 6 pc in the Model B results are at the contact discontinuity for that run and arise from the discontinuity in velocity at initialization. For Model A, the $2 M_{\odot}$ of ejecta is all interior to 2.5 pc and the discontinuity has been erased by thermal conduction.

² Note that sharpness of the central brightness peak varies among this class of supernova remnants, with W44 and W28 having sharper peaks than 3C391 or W63 (Rho, 1997).

At 1 cm^{-3} , a radius of 4 pc contains $8 M_{\odot}$. Thus, the mass in the central few parsecs of W44 should clearly be heavily contaminated by the stellar ejecta and enriched in metallicity. Instabilities and turbulent mixing potentially offer the possibility of diluted enrichment through much of the roughly $100 M_{\odot}$ in the hot interior. With an enrichment that decreased with radius, the observed radial profile could be matched. What is surprising, however, is how little enrichment could be tolerated in conductive models before the prediction exceeds the observed brightness. For example, the factor of only 5 enhancement over solar abundances in the $2 M_{\odot}$ of ejecta in Model C increases the line emissivity by a factor of 5 in the inner $2.5 \text{ pc} \sim 4'$, and the central surface brightness by about a factor of 2. More than that would be too much unless compensated by modeling a less dense remnant at greater distance or by a reduction of thermal conductivity. Interestingly, the nonconductive models do not suffer from this limitation; they are so hot in the interior that their (already weak) central emission is mostly due to bremsstrahlung and does not increase substantially. Our tentative conclusion is that the elemental abundances of the ejecta must be accommodated much more realistically before the very centermost region can be addressed. A major part of getting that right will be to manage to hide most of the metallicity, in clumps that were never fully heated, in overdense regions which have already managed to cool, or in dust grains.

Cloudlet Evaporation

Setting aside concerns over the ejecta, we imagined a hybrid model, including thermal conduction in the interior (represented by our hydrocode results) and cloudlet evaporation as parameterized by White and Long (1991). In particular, we looked for possibilities in which evaporation contributes to the brightness only in the central few parsecs. We expected that somewhat lower mass loss from evaporating clouds would be required than estimated by Rho *et al.* (1994) or Jones *et al.* (1993). This possibility is not clearly successful, however. Figure 4 of White and Long (1991) shows that the effect³ of an evaporating population of clouds is to increase the column emission measure for projected radii less than about 0.65 to 0.85 of the shock radius (depending upon the chosen evaporation parameters). Only in the extreme case of an infinite evaporation time scale and very large ratio of preshock cloud mass to preshock intercloud mass is the contribution in the center significantly greater than that at medium impact parameters, and even this extreme case is not significantly more centrally peaked than our models, owing to their flat central distributions of density and pressure. Their model as it stands does not seem to contribute usefully to peaking of the distribution.

Restriction of Dust Destruction to Sputtering

Restricting dust destruction to thermal sputtering in the hot gas was considered in Model F, using the method described in Smith *et al.* (1996) to calculate the rate. We found that dust destruction was greater in the center of the remnant, providing a relative enhancement of the abundances of the hot gas, but that the effect was not strong enough to match the peaking of emission in the center of the remnant. Additionally, since the plasma with depleted abundances is less efficient at X-ray emission, the total flux was reduced to about 50% of that of Model A with the same absorption column density. A more careful study including dust destruction processes in the shock and revision of absorption based on the new model spectrum might be more successful overall. In any case it is somewhat dangerous to assume that the elemental abundances everywhere in the hot interior are undepleted. Thermal sputtering alone is insufficient to destroy the dust completely.

How Can a Remnant be Shell-Like in Radio and Centrally Bright in X-rays?

Like W44, our Model A does not appear limb brightened. And, as with our 2d model, this absence of limb brightening is not dependent on preferential absorption of softer x-rays emitted by the cooler material further out, although that effect certainly shapes the profile somewhat. The density rises toward the outside, and there is considerable emission from material there, but not at x-ray wavelengths. The reason that our model of W44 is centrally brightened in x-ray emission is that the explosion occurred in a sufficiently high density that the X-rays emitted by the interior are still bright when the outer part of the remnant becomes too cool to detect. Using our rule of thumb that, at the shell formation time, the central density in the presence of thermal conduction should be about 0.13 of the ambient density, explosion site densities in excess of a few cm^{-3} should lead to radiative remnants (shell like in radio continuum) with observable x-ray emission from the interior.

³ The environment for their work was a model which included thermal conduction only in the the evaporation of clouds, while our picture assumes thermal conduction everywhere. Perhaps the two views do not mix as easily as we have assumed in this discussion.

Without thermal conduction, x-ray emission is confined to an interior thick shell-like region, as in our Model B, with temperature and density similar to Model A. Harrus *et al.* (1997) showed that such a model would not necessarily show its shell like character in projection, although our Model B does. Although Model A works better, it still fails to address the central peak without further complications.

6.2.3 X-ray Spectrum

X-ray Spectrum

The observed spectra from the ROSAT PSPC and *Einstein* SSS are compared with Model A in Figure 15a and b. Because the SSS had a 6' diameter field of view, the model SSS spectrum was calculated using a cylindrical slice through the center of the remnant while the PSPC spectrum used the entire remnant. Because our models are somewhat underluminous in the center and the *Einstein* SSS and ROSAT PSPC have different fields of view, the normalization for each instrument fit was allowed to vary independently. The total fit to both datasets has a reduced χ^2 of 2.0. Most of the χ^2 comes from the *Einstein* SSS data because the model has too little emission in the Si XIII complex around 1.85 keV. The best fit normalizations turned out very well. The model was underluminous compared to the *Einstein* SSS observations, by 36%. For the PSPC, however, Model A predicts 25% more emission than is seen. Since the SSS had a smaller field of view than the PSPC, this result suggests the central region is brighter than this model predicts. The best fit N_H was $1.89 \times 10^{22} \text{ cm}^{-2}$, a value we've chosen to use for all other comparisons, and which concurs with the 2d model conclusions.

The spectrum for Model C with its enhanced abundance ejecta is shown in Figure 16. The column density fit to the PSPC and SSS data is barely changed ($N_H = 1.88 \times 10^{22} \text{ cm}^{-2}$), but the PSPC response to the model now implies the model is 35% too bright. The model also overestimates the *Einstein* SSS emission, predicting 23% more emission than observed. The overall spectral fit to the data is slightly worse; the reduced $\chi^2 = 2.5$, and again the worst part is the fit to the *Einstein* SSS at 1.85 keV.

Ionization Equilibration

Rather than a thorough exploration of collisional ionization equilibration (CIE) of the diffuse interior in the presence of substantial conduction, we content ourselves with a comparison of the x-ray spectra of Model A, with and without the assumption of CIE, to learn what instrument characteristics are required to distinguish between them. Although we have the complete nonequilibrium ionization (NEI) balance saved for each parcel, we can calculate the corresponding CIE model as well. We did two different model fits. In the first case, we allowed both the overall normalization and the absorbing column density N_H to vary. In this case, the best fit value (with reduced $\chi^2 = 1.89$) had $N_H = 2.03 \times 10^{22} \text{ cm}^{-2}$. The PSPC model was 10% underluminous, while the *Einstein* SSS model was underluminous by a factor of 2. Figure 17 compares this equilibrium model with the nonequilibrium spectra as seen by the ROSAT PSPC and the *Einstein* SSS. For the second case we held the column density fixed at $N_H = 1.89 \times 10^{22} \text{ cm}^{-2}$ and fit the data. In this case the fit was extremely poor (reduced $\chi^2 = 4.7$). The PSPC model, unsurprisingly, is now overluminous by 14% while the *Einstein* SSS model emission is still a factor of 1.82 underluminous.

The *Einstein* SSS spectrum shows three strong peaks, which were identified by Jones *et al.* (1993) to be from Mg XI (1.34 keV), Si XIII (1.85 keV), and S XV (2.45 keV). These ions are all part of the helium isosequence, and each corresponds to the strong helium triplet of forbidden, intercombination, and resonance lines. (See Gabriel *et al.* (1991) for a fuller discussion of these lines in the context of O VII.) The largest difference between the CIE and NEI models is that in equilibrium, the dominant stage is helium-like. In the NEI model, the gas has been over-ionized by the shock, and slowly recombines from the hydrogenic ion to the helium-like one. In this case the forbidden line of the triplet will be pumped by the recombination. A resolving power $E/\Delta E > 60$ would be needed to separate these lines. The hydrogenic ion, however, also has emission lines—specifically, the Ly α lines, which are at 1.47 keV, 2.01 keV, and 2.62 keV respectively for Mg XII, Si XIV, and S XVI. In the recombining plasma, these lines may be an order of magnitude stronger than at equilibrium. Energy resolution of only $E/\Delta E > 11$ is required to distinguish them. The *Einstein* SSS has a FWHM of $\sim 0.14 \text{ keV}$ (Giaconi *et al.* 1979) which would allow at best a marginal limit be placed on these lines.

Table 5: The observed and calculated emission in the soft and hard ROSAT bands.

Band	Observations	Model A	Model B	Model C
soft (R4+R5+R6)	2.026 ± 0.069	2.22	0.923	2.37
hard (R7)	1.838 ± 0.067	2.12	0.915	2.28

Total Count Rate

Table 5 shows the total count rates in the two ROSAT PSPC bands, soft (R46) and hard (R7), for the observations and the three different models. The observational values are extracted via the method of Snowden *et al.* (1996), while the model values are calculated using a response matrix generated through FTOOLS. The assumed N_H was $1.89 \times 10^{22} \text{ cm}^{-2}$ for models A, B, and C. Using Xselect (Turner, 1996) and XSPEC (Arnaud, 1996) to reduce the data gives an $\sim 10\%$ higher count rate for these bands than the Snowden *et al.* (1996) method. The reason for this discrepancy is not completely understood, but is probably due to the improved background subtraction done in the Snowden *et al.* (1996) method.

Reduction of Thermal Conductivity

As discussed in Section 4.4, there is some controversy regarding the efficacy of thermal conduction in the presence of a magnetic field. In order to explore the effect of lowering the thermal conductivity, we calculated Model E, identical to Model A except with the thermal conduction constant β reduced to 10% of the standard value of $6 \times 10^{-7} \text{ cgs}$. This model has a higher central temperature ($T_c = 9.8 \times 10^6 \text{ K}$), lower central electron density ($n_c = 0.51 \text{ cm}^{-3}$), and steeper gradients than does case A. As a result, the emission spectrum (Figure 18) is harder. The final fit is poor, with a reduced $\chi^2 = 3.4$. The PSPC model is overluminous by 5% while the SSS model is underluminous by a factor of 2.13. The best-fit value has $N_H = 1.78 \times 10^{22} \text{ cm}^{-2}$, slightly less than for the best fit to Model A.

7 Discussion

The methodology of this investigation has been the application of analytic theory as far as possible, followed up with numerical hydrodynamic modeling to verify the details. The main successes are summarized in the abstract, while the overview of the paper’s organization and an index to the various results are provided in the introduction. A number of analytical tools, some in review and some unique and new, were presented in §3. The synchrotron flux available from the van der Laan mechanism is discussed in §3.4.1, with the main result in Equation 22. Proof that thermal conduction should lead to a fixed ratio of central to ambient density at the cooling epoch, and the dependence of that ratio on conductivity appear in §3.3. The theoretical section is summarized in §3.9, and a schematic of the basic model appears in Figure 1. The remainder of this section provides a brief summary as a backdrop for a fuller confrontation with a few key points. Each subsection presents successes first, followed by caveats, and ideas for observations.

7.1 Energy, Environment, Age

The model we have presented for W44 is the remnant of a 10^{51} erg supernova. It occurred in a region with an explosion site density of about 6 cm^{-3} and a density gradient whose scale height equals one remnant diameter at the present time. Our hydrodynamic studies assumed a smooth density distribution, but there must be irregularities to achieve the shell corrugation implied by the filamentary radio continuum emission pattern. The age of the remnant is that of the associated pulsar, about 20,000 years.

None of observations we interpreted required the remnant to be interacting with dense molecular material in the vicinity. The model’s dense end has a preshock density of only 10 cm^{-3} . The remnant itself shows no significant morphological relationship between its radio continuum and the oft mentioned Wooten cloud. It seems to be in a region with surrounding molecular clumps, but is not definitely encountering any. That said, we stress two caveats. First, the shell corrugation is a

consequence of a lack of smoothness of the ambient medium on 1 to 10 pc scales and we have not explored the degree of density contrast required to generate that corrugation. Second, we found that the gamma ray flux could be raised to the observed level from the vicinity if the cosmic rays in the dense shell were interacting with 2 to 4 times as much mass as we predict. It is not known that the gamma rays do derive from the remnant, but, if it can be shown that the eastern shell is the source and has the presently quoted flux, it may be necessary to revisit the possibility of dense inclusions or high contrast irregularities.

7.2 The Hot Interior

We assumed that thermal conduction in the hot interior occurs at its unquenched rate, limited by saturation (§4.4), with the result that the minimum interior density drops only to about 13% of ambient and the central temperature is limited to about 6×10^6 K. These conditions produce the observed central x-ray emission (§3.3, 5.2.1, 6.2.1). The remnant's temperature is low in the outer parts, in part because it has become radiative. As a result, its center filled x-ray morphology is not accompanied by a bright shell, even prior to absorption (§5.2.4, 6.2.2). After absorption it yields approximately the observed intensity and spectrum.

At normal abundances, the x-ray emission from the remnant interior is calculated to arise from approximately $30 M_{\odot}$. One expects that the enriched stellar ejecta should have distorted the spectrum, the surface brightness distribution, and the overall intensity. And yet, our basic model reproduces most of the spectral detail, missing only noticeably in the strength of the Si XIII complex around 1.85 keV, and provides essentially the correct total count rate (§6.2.3).

The only hints that the ejecta play a role are in the surface brightness distribution (§6.2.2). That distribution has three characteristics of interest. Unlike that provided by our basic model, the radial distribution has a relatively sharp central peak and is concave upward elsewhere. In addition, the image is somewhat lumpy, a characteristic which may have contributed to the idea that there are discrete evaporating clouds associated with the emission. Some of this distribution may arise from variability in the absorption screen, but we are inclined for reasons given in the text to believe that at least the central peaking is real (§2.5). Our ad hoc experiment with moderately enhanced abundances in the stellar ejecta (§6.2.2) easily provided sufficient additional central emission, but far more can be done to clarify the situation. The observed distribution and spectrum depend at least on the abundance distribution in the stellar envelope, on the wind activity of the star in shaping its environment prior to the explosion, on the degree to which dust formation extracts elements from the gaseous phase, on the instabilities in the wind bubble and explosion activity tending naturally to form lumps, on the potential for some of those lumps to cool and return to high density, on the radial mixing profile of the interpenetrating fluids of ejecta, wind and ISM, on the thermal conductivity within the stellar wind bubble and in the hot interior of the remnant, on the electron-ion thermal equilibration rate, on the dust destruction rates, and on the stellar density profile and the irregularities in the medium which will influence the focussing and location of the reverse or reflected reverse shock at the present time (§5.2.1).

Improved imaging and spectra of W44 X-rays can very much clarify the constraining information, particularly on the ionization history and current temperature of the gas (§6.2.3), but it would be premature to suppose that existing modeling efforts have been sufficient for meaningful comparison with data taken from the central third of the remnant. A great deal more careful work lies ahead, with major difficulties and dangers in the sophistication needed in approximating the interrelated phenomena. The good news is that many models of the details will be totally unacceptable, producing far more X-rays with very much the wrong spectra. The payoff will be multiparameter constraints on the possible characteristics of the star, its interaction with the surroundings, and on the degree of thermal conduction allowed or required. As for the concavity of the angle averaged surface brightness distribution, modelers must take care to be sure that scattering of the X-rays by intervening gas is included in their final comparisons.

7.3 The Shock and Dense Shell

The model remnant's shock shows cooling effects everywhere, but a dense shell has formed only on the higher density end (Figure 1 and §3.1, 3.7, 5.2.1). With that end tilted somewhat away from

the line of sight, the half shell can be seen as a receding distribution of HI whose velocity structure agrees with observations (§5.2.2). The radio continuum arises from the dense shell, via synchrotron emission in an approximately 200 μG field (§3.4.1, 5.2.3), with its filamentary structure due to local tangencies of the corrugated shell with the line of sight (§5.2.3). The shell should also be a source of gamma rays, from both bremsstrahlung by the CR electrons and π^0 production by the protons, at about 1/4th to 1/2 the rate measured by EGRET as arising from the vicinity (§3.6).

The radiative shock and ongoing shell formation generate the usual radiative remnant's spectrum, in UV, optical, and IR, with rates that correspond to recent observations of H α , [SII], and 63 μm [OI] (§3.5). Much of this emission is associated with the edge of the dense shell and should correlate well with the filamentary structure, though some could be more diffusely arranged in the remnant's equatorial belt where shell formation is currently strongest. Both aspects are consistent with existing observations, though in the optical the observations are made through a variable screen of several magnitudes of foreground extinction (measured by the absorption column of the x-ray spectrum).

Because the filaments arise geometrically from tangencies to the shell, any correlated line emission should appear at the local rest velocity (expansion is perpendicular to the line of sight), a characteristic that distinguishes filaments due to tangency from those due to actual filamentary (rope-like) structures. This velocity null for the filaments has been confirmed in the associated OH maser emission (Frail, 1998, private communication), but should be checked in H α because of possible disagreements over the origin of the maser emission.

Unfortunately, the large and variable optical depth to W44 degrades the information available from optical intensity studies. But a velocity resolved study of the H α , or of other spectral components potentially associated with the shell and or evaporating clouds, could be useful in several ways. We expect emission from the existing shell, from the immediate surroundings, and from the equatorial belt where shell formation is in progress. The shell component should strongly resemble the HI distribution in velocity and space, but can likely be detected from the approaching (shell forming) side as well as from the receding side, and traced to the shell edge at low velocity, the latter not being possible in 21 cm due to confusion with other material along the line of sight. In addition to the important verification of the the zero radial velocity of the filamentary emission, a search is needed for a possible emission component associated with the x-ray bright spots, as would be expected from evaporating (or cooling and condensing) lumps. Perhaps most interesting is the possibility of seeing emission from gas which is just joining the inner surface of the shell. If the cooling is sensitive and therefore somewhat erratic, the condensation flow could be irregular and have some components expanding at a noticeably higher speed than the shell they are overtaking.

We found that the van der Laan mechanism, sweeping up of ambient cosmic rays and magnetic field and compression of both into the dense shell, can plausibly provide both the observed spectrum and intensity of the radio synchrotron emission (§3.4.1), but there was a hidden difficulty with the formulation that amounted to assuming that the ambient CR electron density there is about 4 times greater than that estimated for the solar vicinity. This is not necessarily a problem. Attempts to measure the synchrotron emissivity of the general ISM have been difficult and seem to have both significant uncertainty and genuine variability. In addition, W44 is in an active region at the base of the Aquila supershell (Maciejewski *et al.*, 1996) and could very well be encountering an enhanced CR population. Other important processes potentially contributing to the cosmic ray electron population are discussed in §3.4.2. A caveat in our analysis is that our use of the viewing-angle averaged synchrotron radiation formula may have been misleading in the presence of the orderly tangential magnetic field seen in W44.

The extremely high angular resolution of the OH maser locations and their relationship to radio continuum ridges and bright spots (Claussen *et al.* 1997) appears to us to require the masers to arise from the leading edge of the dense shell, i.e. at the trailing edge of the cooling and recombination zone of the radiative shock, with masering occurring tangential to the shell's outer surface so that it is observed only along the filaments. Consistently, the magnetic field measured via the maser emission is just that found for the shell in our model (§3.4.2), and as noted above, their radial velocities are at the local rest velocity. We are not aware of models for shocks in such low density gas to test for the presence of sufficient OH, or of maser pumping models for this nonequilibrium environment, but we note that the models by Hollenbach and McKee (1989) for shocks in denser gas do have a significant abundance of OH on leaving the photoionization/recombination plateau,

and show a local peak in the OH emission at a column density behind the shock of about 10^{20} cm^{-2} , where the temperature is dropping rapidly through 1000 K. This result may not be sensitive to the initial density (McKee, private communication 1998); and the required column density is achieved in our model. The anticipated neutral density in this region is a few hundred cm^{-3} , limited by the magnetic pressure. The observations cry for studies of 100-150 km s^{-1} shocks into densities of 10-100 cm^{-3} and their potential for creating molecular gas and generating OH maser activity tangential to the shock surface, possibly with the pumping arising in transience of the material (e.g. formation of the OH in excited states). The solution could be elusive, however, based on the observation that there are many small maser spots but far more filamentary regions without masering, at least not beaming towards us.

Our predicted shell mass would also agree better with the HI data if much of the shell were molecular (§5.2.2). If there is a strong molecular line which is insensitive to reddening and associated with radiative shocks, perhaps from the fluorescence region at the outer edge of the dense shell, a line not present in the ambient medium or foreground molecular gas, it could provide an excellent probe of the shell's actual extent and velocity structure. The model's overall shell mass is about $450 M_{\odot}$ of which perhaps half is molecular. If it can be shown that the molecular mass in the shell is substantially larger than this, perhaps in structures related to the shell corrugation, it could also remove the apparent discrepancy between our model's gamma ray production and the EGRET measurements, while requiring only some adjustment of the ambient density distribution in the next generation of models.

7.4 Distance and Fine Tuning

The oft-quoted distance for W44 is 3 kpc, but we reviewed this assessment in §2.2, concluding that the appropriate modern number is 2.5 to 2.6 kpc. Our theoretical attempts to choose parameters that would produce the correct angular size at this distance failed slightly, forcing us to describe the model characteristics for a distance of 2.2 kpc. It is not impossible that the remnant is this close, and within the uncertainties of such modeling, the differences are inconsequential. Nevertheless, it may be worth comment. Section 3.8 introduced scaling laws for adjusting our results to remnants located at different distances. Two scalings are presented, exact Sgro-Chevalier scaling, and approximate scaling for constant explosion energy. For Sgro-Chevalier scaling to 2.5 kpc, we found that the only appreciable changes were a 12% reduction in the x-ray surface brightness and luminosity, and a factor of 1.3 increase in explosion energy and shell mass. The increase in explosion energy is the only uncomfortable part, leading us to favor the more approximate scaling. In that case, the only appreciable change is the reduction of the x-ray surface brightness and luminosity by a factor 0.53. Recalling that Model A was about 25% overluminous leads to no worse overall agreement. However, considering that a significant part of the total x-ray emission may be associated with the elementally enriched center as discussed above, this increase in distance is an improvement, allowing a greater degree of enrichment of the interior without having to resort to a reduced thermal conductivity for compensation. With this model, the explosion site density would be only 4.6 cm^{-3} and the age 23,700 years. Both are intermediate between Model A and the parameters found by Harrus, *et al.* (1997).

7.5 Relationship of the Model to Other Remnants

Finally we would like to remark on the possibility of generalizing this model to other remnants. To have both a strong radio shell component and an interior which is luminous in thermal X-rays requires both a substantial compression of the dense shell, and a substantial interior density and pressure. In §3.4.1 we found that the radio synchrotron surface brightness shortly after shell formation should be roughly proportional to Rp_{shell} , while in §3.8 we found the x-ray surface brightness of the interior proportional to $Rp_{interior}^2$. We have not explored our hydrodynamic models to learn how rapidly these surface brightnesses fade as the remnant continues to expand, but we expect a very considerable drop in the x-ray emission by the time it has grown very far. The radio continuum is less sensitive in the first place, and will drop more gradually because it rises with cooled mass and because remnants in inhomogeneous media have shell formation occurring over part of their surface for a protracted period of time. We naturally expect then that remnants with radio

shells will be more common than those with x-ray luminous interiors, and can concentrate on the conditions needed for the latter. At shell formation, when the outer edge is too cool to radiate in x-rays, the surface brightness of the interior should be roughly proportional to R_{cool}^{-5} . In that case it is clear that the class of remnants to which our model applies should have a very steep dropoff of surface brightness with size at shell formation, as well as with size after shell formation. Using §3.2 to relate shell formation radius to ambient density, we infer that the x-ray surface brightness of the interior at shell formation is approximately proportional to n_o^2 . As we have not explored the effects of any presupernova wind on the later internal structure of the remnant, this result may be somewhat naive, but our tentative expectation is that an x-ray bright interior for a supernova remnant of typical energy will occur only when the explosion occurs in an extended region of higher than average interstellar density.

For contrast, consider the Cygnus Loop. Its radio continuum derives largely from compressed material behind roughly 100 km s^{-1} radiative shocks moving into recently encountered large scale clouds of density roughly 8 cm^{-3} , not so different from W44. Its flux is similar to W44's, its distance about a third as great, so its radio continuum luminosity is lower by about a factor of 10. The remnant volume is about 4 times that of W44, so the mean internal pressure is about 4 times lower. The brightest x-rays are associated with the interaction with the large dense clouds, and are found just inside the radiative shocks. The distribution of the more diffuse x-rays, however, resembles that expected from a Sedov structure with ambient density 0.16 cm^{-3} . We therefore estimate the interior density to be about 1/30th that of W44 and the interior temperature about 7.5 times greater, 4 to $5 \times 10^7 \text{ K}$. Continuing to assume that the abundances are unaffected by the ejecta, which provides the correct count rate for W44, and consulting our ROSAT PSPC counts per emission measure tables with negligible absorption for the Cygnus Loop and the amount found above for W44, we conclude that the observable (after absorption) surface brightness of the Loop interior should be lower by roughly a factor of 10. That reduction appears modest until compared with the radiation from the 30 times denser edge. At a temperature of $2.4 \times 10^6 \text{ K}$, the "shell" emission is about 2 orders of magnitude brighter in projection across the center of the remnant and much brighter yet as seen near the edge. Although there are radiative shocks on part of the surface of the Cygnus Loop, much of the evolution is in low density and is very far from having the low edge temperatures associated with incipient cooling and shell formation. Only an instrument with sensitivity to very hot gas could discern the high temperature interior from the softer "shell" emission.

There are two ways of creating much larger remnants with x-ray emitting interiors. One, explored by Shelton (1998) in the context of halo and interarm supernovae, simply involves exploding in a very low density (0.01 cm^{-3}) and waiting for the edge temperature to drop too low to show up as an x-ray shell. The other was explored in Smith and Cox (1998) in connection with modeling the Local Bubble. A second supernova within the cavity of an earlier remnant can reheat the interior and bring it back into x-ray emission. And that emission can last a substantial length of time, possibly making unlikely events yield not uncommon objects in the sky. The two approaches are not entirely dissimilar in that the Local Bubble model starts with a higher ambient density and uses the first explosion to create the low density into which the second explosion initially evolves. One difference is that the multiple explosion model has denser surroundings which slow the shock and lead more quickly to a low temperature edge.

7.6 Closing Remarks

This study was undertaken to show that the characteristics of a heavily observed and very exciting supernova remnant, W44, could be understood in the context of a very simple model, a model which did not invoke evaporating clouds in the center, or blast wave accelerated clouds to make the observed HI, or interaction with a dense molecular cloud environment, or diffusive shock injection and acceleration of cosmic rays. The required features were a relatively dense ambient environment, a significant density gradient, shell corrugation due to moderate irregularities in the ambient medium, betatron acceleration of the ambient cosmic ray population, and a significant amount of thermal conduction in the hot interior. It was hoped that the observed intensity of x-rays from the hot interior would then finally give us a relatively conclusive measure of the magnitude of the thermal conductivity.

The model was wildly successful, but not without its disappointments. We were able to show that compression of the ambient cosmic rays could lead to approximately the correct radio continuum flux and spectrum, and to a significant contribution to the gamma ray intensity, but could not show that there is no room left for diffusive or other forms of acceleration. We found that the intensity and spectrum of the interior x-ray emission were consistent with unquenched thermal conduction, but could not convince ourselves that the metallicity contamination by the ejecta and preexplosion evolution could be neglected. As a result we are less confident in our determination of the magnitude of the thermal conductivity in the hot interior of the remnant. On the positive side, the need for clouds and clumps in the remnant interior vanished, as did any hint of interaction with dense molecular clouds. The shell emission characteristics were in beautiful agreement with the measurements, and comparison with the OH maser observations led to the ideas that the shell could be largely molecular and that the trailing edge of the cooling region is the site of the masering activity.

8 Acknowledgements

We would like to acknowledge useful advice, conversations, and assistance from, with, and of Namir Kassim, Bob Benjamin, Rob Petre, Jeonghee Rho, Dale Frail, Linda Sparke, Pat Slane, Blair Savage, and John Raymond during various times of the long course of this project. We are also grateful to Bon-Chul Koo for providing the HI data for comparison with our model.

This work was supported in part by NASA Grant NAG5-3155 to the University of Wisconsin-Madison. RLS and RKS were also supported by grants from the National Research Council while at the NASA/Goddard Space Flight Center, in the Laboratory for High Energy Astrophysics, and the Laboratory for Astronomy and Solar Physics, respectively.

TP and MR benefited from the Polish Committee for Scientific Research grant 2.P03D.004.13. The 2-D simulations reported in this paper were conducted at MPG Computer Center in Garching and Interdisciplinary Center for Computational Modelling (ICM) in Warsaw.

This research has made use of data obtained through the High Energy Astrophysics Science Archive Research Center Online Service, provided by the NASA-Goddard Space Flight Center.

9 References

- Arnaud, K.A. 1996, *Astronomical Data Analysis Software and Systems V*, eds. Jacoby G. & Barnes J., p17, ASP Conf. Series volume 101
- Berger M.J., Colella P. 1989, *J. Comput. Phys.*, 82, 64
- Bloemen, H. 1989, *ARAA*, 27, 469
- Caswell, J.L., Murray, J.D., Roger, R.S., Cole, D.J., & Cooke, D.J. 1975, *A&A*, 45, 239
- Chevalier, R.A. 1973, PhD thesis, Princeton University
- Cid-Fernandes, R., Plewa, T., Różyczka, M., Franco, J., Terlevich, R., Tenorio-Tagle, G. & Miller, W. 1996, *MNRAS*, 283, 419
- Clark, D.H., & Caswell, J.L. 1976, *MNRAS*, 174, 267
- Clark, D.H., Green, A.J., Caswell, J.L. 1975, *Australian Journal of Physics Astrophysical Supplement*, 37, 75
- Claussen, J.M., Frail, D.A., Goss, W.M., & Gaume, R.A. 1997, *ApJ*, 489, 143
- Clemens, D.P. 1985, *ApJ*, 295, 422
- Colella P., Woodward P.R. 1984, *J. Comput. Phys.*, 59, 264
- Cowie, L.L. & McKee, C.F. 1977, *ApJ*, 211, 135
- Cox, D.P. 1970, PhD thesis, UC San Diego
- Cox, D.P. 1972a, *ApJ*, 178, 143

- Cox, D.P. 1972b, ApJ, 178, 159
- Cox, D.P. 1986, ApJ, 304, 771
- Cox, D.P. 1996, "Guide to Modeling the Interstellar Medium," in *Astrophysics in the Extreme Ultraviolet*, eds S. Bowyer & R. F. Malina, Kluwer, p. 247
- Cox, D.P. & Anderson, P.R. 1982, ApJ, 253, 268
- Cui, W. & Cox, D.P. 1992, ApJ, 401, 206
- Dame, T.M. 1983, PhD thesis, Columbia University
- Dame, T.M., Elmegreen, B.G., Cohen, R.S., & Thaddeus, P. 1986, ApJ, 305, 892
- deJager, O.C. & Mastichiadis, A. 1997, ApJ, 482, 874
- DeNoyer, L.K. 1983, ApJ, 264, 141
- Dickel, J.R., & DeNoyer, L.K. 1975, AJ, 80, 437
- Dickel, J.R., Dickel, H.R., & Crutcher, R.M. 1976, PASP, 88, 840
- Dohm-Palmer, R.C. & Jones, T.W. 1996, ApJ, 471, 279
- Edgar, R.J. 1994, personal communication
- Edgar, R.J. & Chevalier, R.A. 1986, ApJ, 310, L27
- Ellison, D.C. *et al.* 1994, PASP, 106, 780
- Esposito, J.A., Hunter, S.D., Kanbach, G., & Sreekumar, P. 1996, ApJ, 461, 820
- Falle, S.A.E.G. 1975, MNRAS, 172, 55
- Falle, S.A.E.G. 1981, MNRAS, 195, 1011
- Frail, D.A., Giacani, E.B., Goss, W.M., & Dubner, G. 1996, ApJL, 464, L165
- Frail, D.A., Goss, W.M., Reynoso, E.M., Giacani, E.B., Green, A.J., Otrupcek, R. 1996, AJ, 111, 1651
- Gabriel, A.H., Bely-Dubau, F., Faucher, P., & Acton, L.W. 1991, ApJ, 378, 438
- Giacani, E.B., Dubner, G.M., Kassim, N.E., Frail, D.A., Goss, W.M., Winkler, P.F., & Williams, B.F. 1997, ApJ, 113, 1379
- Giacconi, R. *et al.* 1979, ApJ, 230, 540
- Goss, W.M., Caswell, J.L., & Robinson, B.J. 1971, A & A, 14, 481
- Grevesse, N., & Anders, E. 1988, AIP Conference Proceedings No. 183, "Cosmic Abundance of Matter", ed. C.J. Waddington, 1
- Kovalenko, A.V., Pynzar', A.V., & Udal'tsov, V.A. 1994, Astr. Rep., 38, 78
- Harrus, I.M., Hughes, J.P., & Helfand, D.J. 1996, ApJ, 464, L161
- Harrus, I.M., Hughes, J.P., Singh, K.P., Koyama, K., & Asaoka, I. 1997, ApJ, 488, 781
- Hester, J.J. 1987, ApJ, 314, 187
- Hollenbach, D. & McKee, C.F. 1989, ApJ, 342, 306
- Jokipii, J.R. & Parker, E.N. 1969, ApJ, 155, 777
- Jones, L.R., Smith, A., & Angellini, L. 1993, MNRAS, 265, 631
- Jones, T.W., Rudnick, L., Jun, B.-I., Borkowski, K.J., Dubner, G., Frail, D.A., Kang, H., Kassim, N.E., & McCray, R. 1998, PASP, in press
- Kahn, F.D. 1975, In Proc. 14th Int. Cosmic Ray Conf. (Munich) 11, 3566
- Kahn, F.D. 1976, A&A, 50, 145
- Kassim, N.E. 1992, AJ, 103, 943
- Kompaneets, A.S. 1960, Soviet Phys. Dokl., 5, 46
- Koo, B.-C., & Heiles, C. 1995, ApJ, 442, 679
- Kovalenko, A.V., Pynzar, A.V., & Udal'tsov, V.A. 1994, Astro. Rep., 38, 78
- Kundu, M.R., & Velusamy, T. 1972, A&A, 20, 237

- Long, K.S., Blair, W.P., White, R.L., & Matsui, Y. 1991, ApJ, 373, 567
- Maciejewski, W., Murphy, E.M., Lockman, F.J., & Savage, B.D. 1996, ApJ, 469, 238
- Maciejewski W. & Cox, D.P. 1998, ApJ, submitted
- McKee, C.F. 1988, personal communication
- Morrison, R., & McCammon, D. 1983, ApJ, 270, 119
- Plewa, T. & Müller, E. 1998, in preparation
- Raymond, J.C. 1976, PhD thesis, University of Wisconsin-Madison
- Raymond, J.C. 1995, personal communication
- Raymond, J.C. & Smith, B.W. 1977, ApJ S, 35, 419.
- Reach, W.T., & Rho, J. 1996, A & A, 315, L277
- Reich, W., Fürst, E., Reich, P., & Reif, K. 1990, Astron. & Astrophys. Suppl. Ser., 85, 633
- Rho, J.-H. 1995, PhD thesis, University of Maryland
- Rho, J.-H. 1997, oral presentation at the Minnesota Meeting on Supernova Remnants (summarized in Jones *et al.* 1998)
- Rho, J., Petre, R., Schlegel, E.M., & Hester, J.J. 1994, ApJ, 430, 757
- Richtmyer, R.D., & Morton, K.W. 1967, "Difference Methods for Initial Value Problems, Second Edition" (New York: Interscience Publishers)
- Rockstroh, J.M., & Webber, W.R. 1978, ApJ, 224, 677
- Rosner, R., & Tucker, W.H. 1989, ApJ, 338, 761
- Sato, F. 1986, AJ, 91, 378
- Schmidt, M. 1965, In *Galactic Structure*, eds. A. Blaauw & M. Schmidt, University of Chicago, Press, p. 513
- Sgro, A. 1972, PhD thesis, Columbia University
- Shelton, R.L. 1998, in preparation
- Shelton, R.L., Smith, R.K., & Cox, D.P. 1995, BAAS, 27, no. 3 (186.5904)
- Slavin J.D. & Cox, D.P. 1992, ApJ, 392, 131
- Smith A., Jones, L.R., Watson, M G., Willingale R., Wood N., & Seward, F.D. 1985, MNRAS, 217, 99
- Smith, R.K., & Cox, D.P. 1998, in preparation
- Smith, R.K., Krzewina, L.G., Cox, D.P., Edgar, R.J., & Miller, W.W. 1996, ApJ, 473, 864
- Snowden, S.L., McCammon, D., Burrows, D.N., & Mendenhall, J.A. 1994, ApJ, 424, 714
- Snowden, S.L. 1994, Cookbook for Analysis Procedures for ROSAT XRT/PSPC Observations of Extended Objects and the Diffuse Background, U.S. ROSAT Science Data Center, Goddard Space Flight Center
- Tao, L. 1995, MNRAS, 275, 965
- Turner, T.J. 1994, "ROSAT data analysis using xselect and ftools", OGIP Memo OGIP/94-010, U.S ROSAT Science Data Center, NASA Goddard Space Flight Center
- van der Laan, H. 1962a, MNRAS, 124, 125
- van der Laan, H. 1962b, MNRAS, 124, 179
- Webber, W.R., Simpson, G.A., & Cane, H.V. 1980, ApJ, 236, 448
- White, R.L. & Long, K.S. 1991, ApJ, 373, 543
- Wolszczan, A., Cordes, J.M., & Dewey, R.J. 1991, ApJ, 372, L99
- Wootten, H.A. 1977, ApJ, 216, 440
- Yanenko, N.N. 1971, The method of fractional steps: The solution of Problems of Mathematical Physics in Several Variables. M. Holt (ed.), Springer-Verlag, New York

10 Figure Captions

Figure 1: Schematic of the Model for W44. Shows annotated section through remnant along plane containing the look direction. Inset shows projection of half shell on the sky.

Figure 2: Number density of each cell in the 2d model, projected on the symmetry axis. The ambient density distribution, partial shell formation, factor of 4 compression at the tenuous end's shock, and the moderately uniform and non-negligible central density are all apparent, as are the regions of finer gridding in the adaptive mesh. The remnant age is 20,000 years.

Figure 3: Surface plot of the 2d model's temperature distribution at 20,000 years. The temperature structure is approximately parabolic, fairly uniform in the central half (in radius) with a steady drop in the outer half to near zero at the edge. On the tenuous end, the post shock temperature of the shock can be seen, along with the trough behind it showing its transition to radiative.

Figure 4: Surface plot of the 2d model's pressure distribution at 20,000 years. The constant central pressure, sloping shoulders in the outer half, strong variations in edge pressure over the surface and the deep trough of cooled but so far uncompressed material can be seen. (The spikes are an artifact of the figure preparation, not a characteristic of the model.)

Figure 5: (*top-right*) HI mass from the simulated SNR viewed at 40° from the symmetry axis. The axis is also tilted toward the southwest. (*bottom-left*) The shaded contours represent the HI brightness observed for W44 between $v_{\text{LSR}} = 135$ and 170 km s^{-1} (Koo and Heiles 1995). The dots represent HI mass from the model for the same velocity interval, assuming a 43 km s^{-1} systemic velocity. (*top-left*) Position velocity diagram for the vertical aperture indicated in the top right panel. (*bottom-right*) Position velocity diagram for the horizontal aperture indicated in the top right panel.

Figure 6: (*top*) Position-velocity diagram of the fast, receding HI gas. The shaded contours represent HI brightness for a cut along $\alpha_{1950} = 18^{\text{h}}53^{\text{m}}30^{\text{s}}$, from Koo & Heiles (1995). The dots represent HI mass for the vertical cut indicated in the previous figure. A systemic velocity of 43 km s^{-1} is assumed. (*bottom*) Same as *top*, for a horizontal cut through $\delta_{1950} = +01^\circ18'$.

Figure 7: Map of the synchrotron emission from the simulated SNR. In the upper right panel, the remnant is viewed at the same orientation as in Figure 5, whereas the lower left panel shows a view perpendicular to the symmetry axis. The upper left and lower right panels show the integrated intensity profiles for the horizontal and vertical slices shown.

Figure 8: Map of the synchrotron emission from the simulated SNR, in which a pattern of radial crinkling has been superposed to illustrate the formation of apparent filaments. The remnant is viewed at the same orientations as in Figure 7.

Figure 9: The 2d model x-ray surface brightness distribution. Includes both hard and soft ROSAT PSPC bands, at a column density of $2 \times 10^{22} \text{ cm}^{-2}$.

Figure 10: The 2d model x-ray surface brightness distribution with no absorption. The 2d model's thermal X-rays are not edge brightened (shell like) even without absorption.

Figure 11: Density distributions of 1d models at 20,000 years. With thermal conduction (Model A, solid line), the electron density is almost 1 cm^{-3} in the center and changes slowly with radius except near the edge. Without thermal conduction (Model B, dashed line) the density is extremely small at the center and increases rapidly with radius. The structures near 11 pc show the early stages of shell formation.

Figure 12: Temperature distributions of 1d models at 20,000 years. With thermal conduction (Model A, solid line), the temperature is 6×10^6 K in the center and changes only slowly with radius except near the edge. Without thermal conduction (Model B, dashed line) the temperature is very high in the center and changes rapidly with radius. The bump at ~ 6 pc is an artifact of the code associated with the contact discontinuity. The structures near 11 pc show the early stages of shell formation.

Figure 13: Thermal pressure distribution of 1d models at 20,000 years, with (Model A, solid line) and without (Model B, dashed line) thermal conduction.

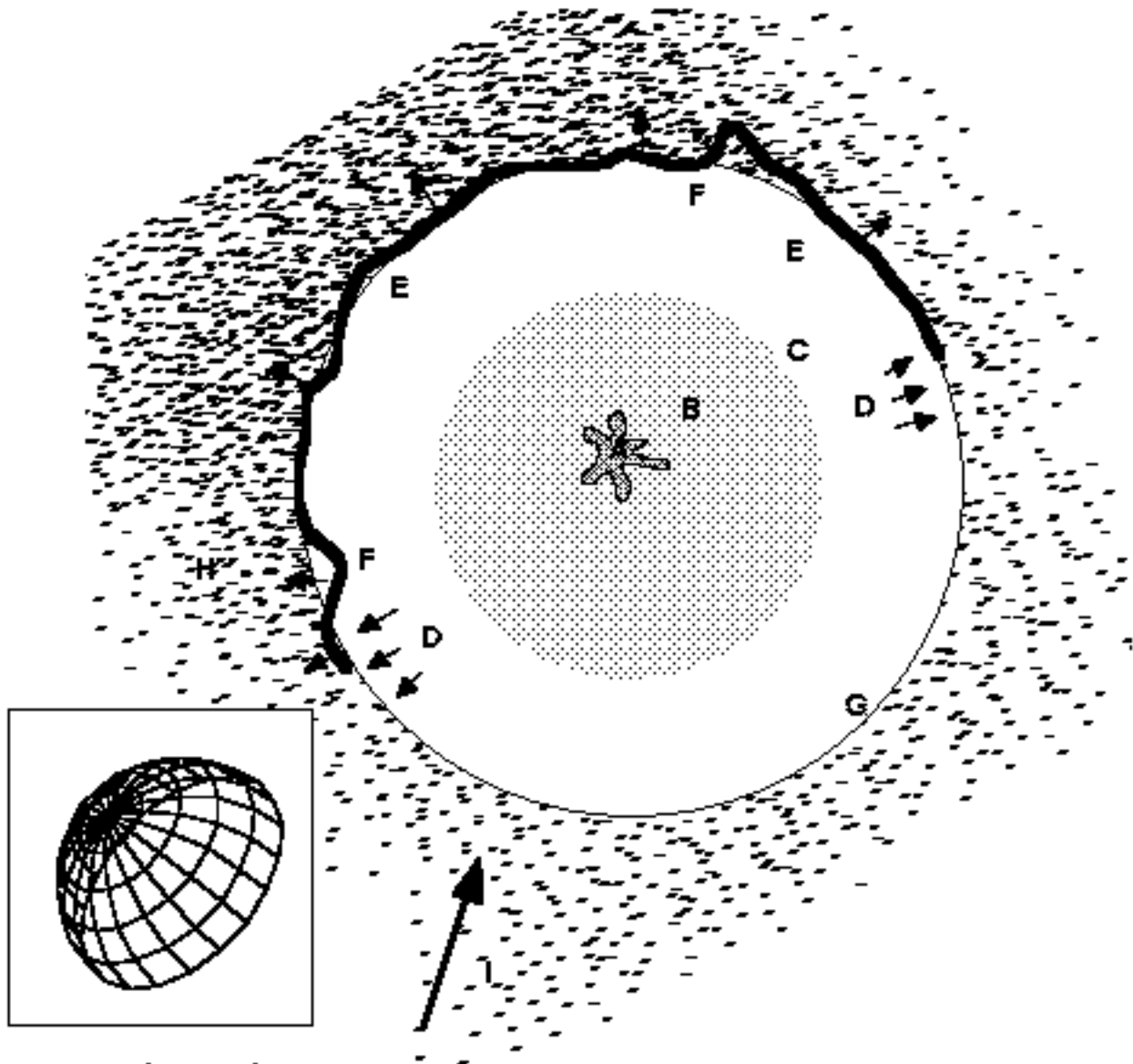
Figure 14: a: The ROSAT PSPC Soft Band (R4+R5+R6, 0.4 - 1.6 keV) count rate for Model A (with thermal conduction, solid line), Model B (without thermal conduction, dashed line), and the observed rates toward the north (cross), east (star), south (diamond), and west (triangle). Models A and B were attenuated with an absorption column density of $N_{\text{H}} = 1.89 \times 10^{22} \text{cm}^{-2}$. b: Same as a, but for the ROSAT PSPC Hard Band (R7, 1.0 - 2.0 keV).

Figure 15: ROSAT PSPC (a) and Einstein SSS (b) spectra fit with Model A.

Figure 16: ROSAT PSPC (a) and Einstein SSS (b) spectra fit with Model C.

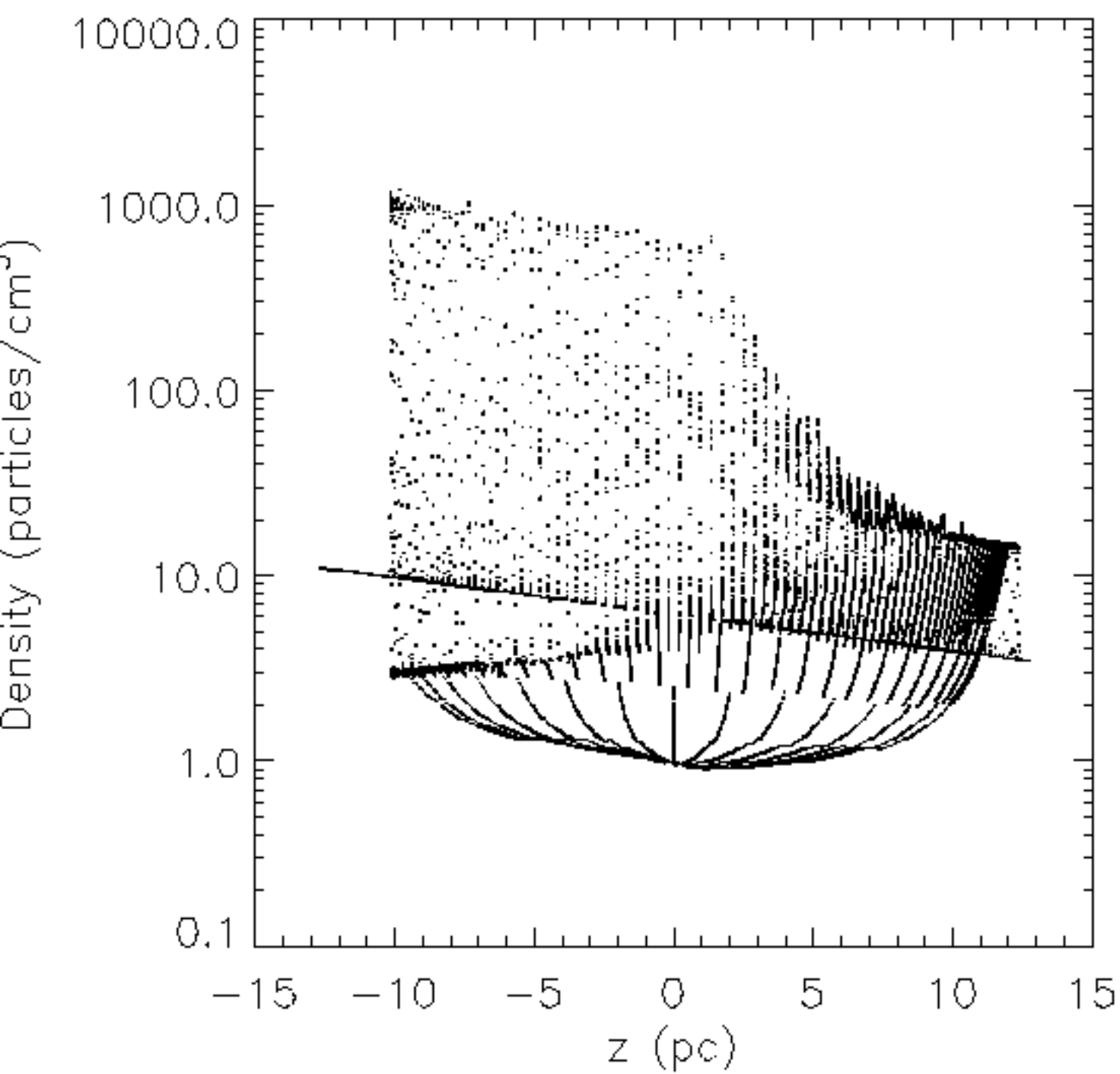
Figure 17: ROSAT PSPC (a) and Einstein SSS (b) views of Model A comparing collisional ionization equilibrium (dashed) and full non-equilibrium ionization (solid). The non-equilibrium model is the same as shown in Figure 15.

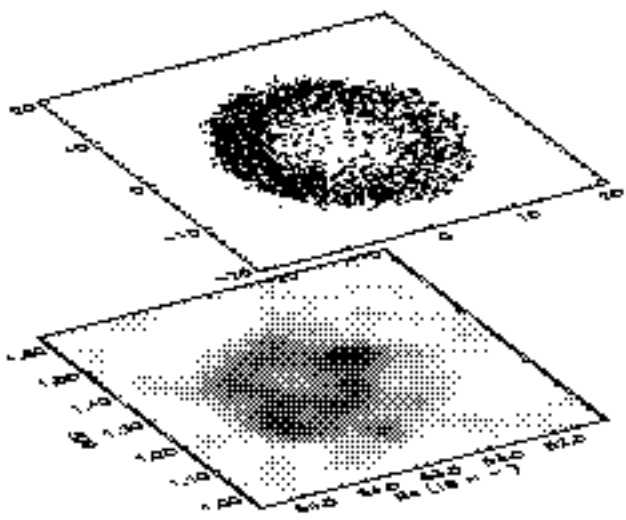
Figure 18: ROSAT PSPC (a) and Einstein SSS (b) spectra fit with Model E, identical to Model A but with the thermal conductivity reduced by 10.

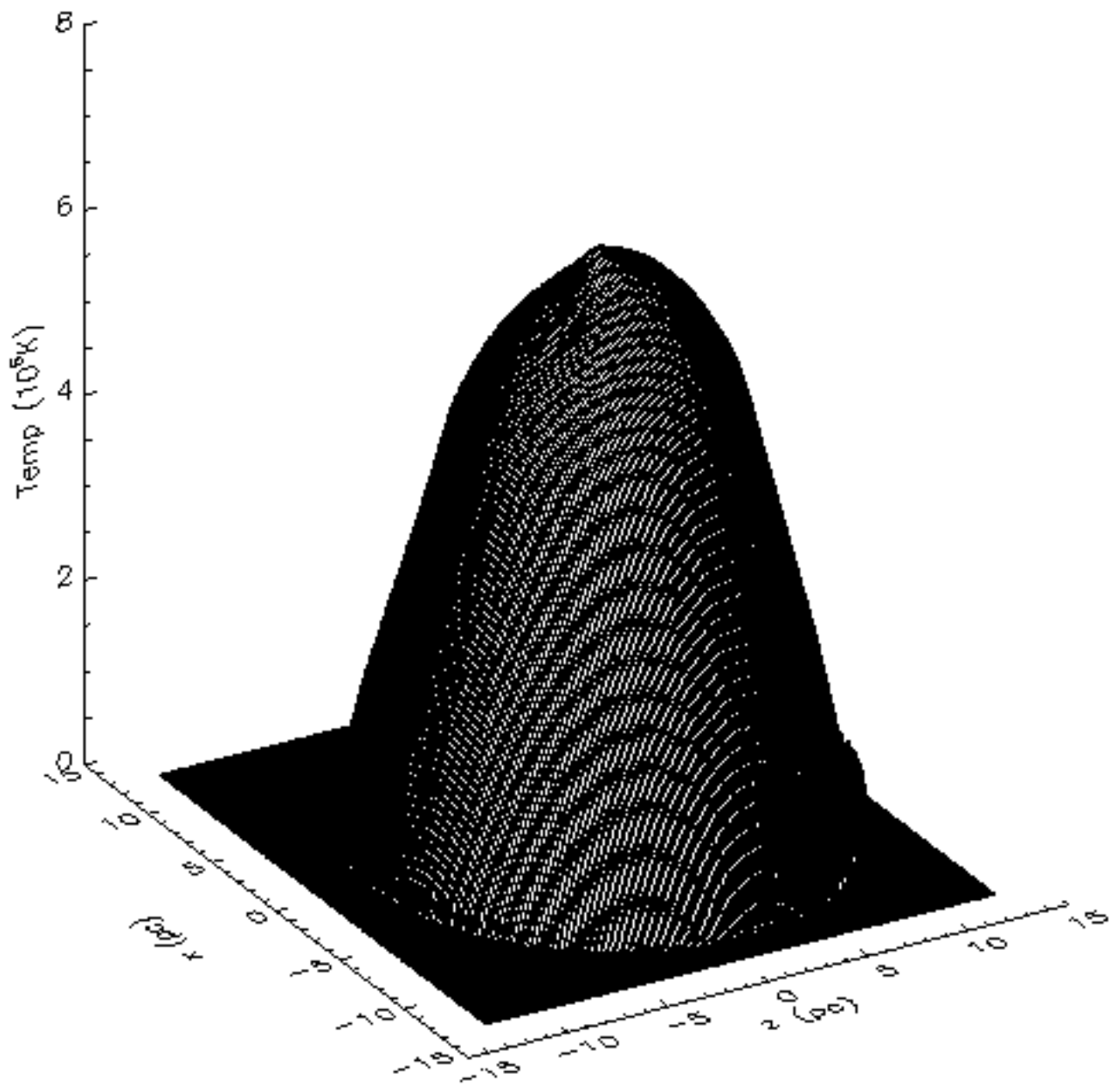


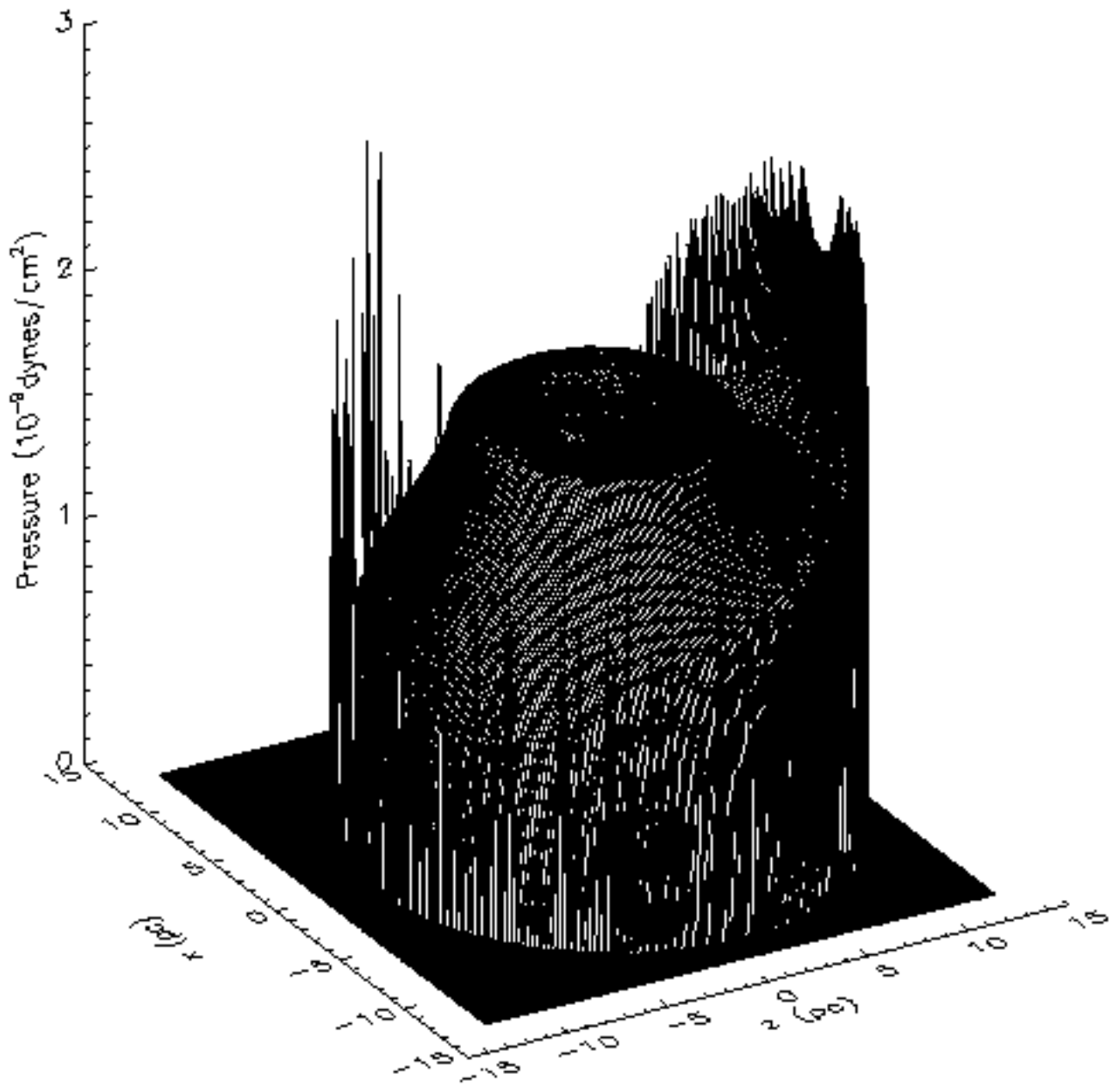
Legend

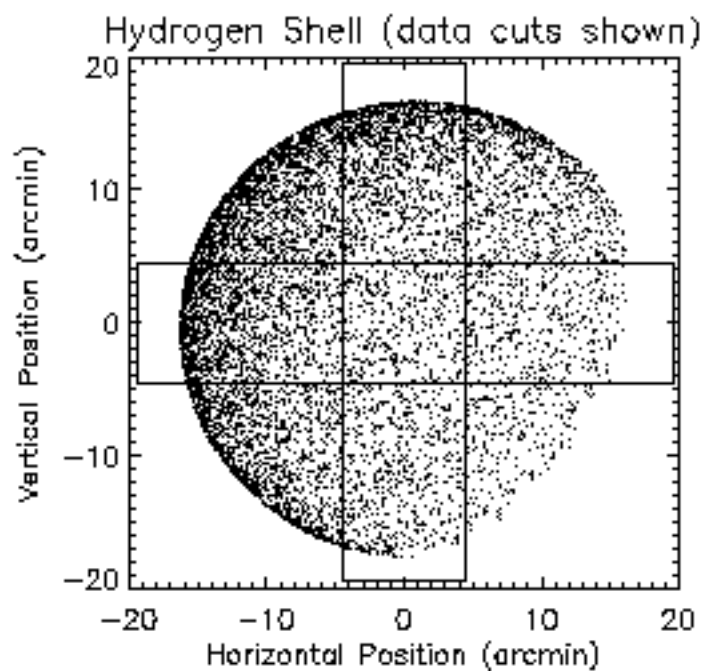
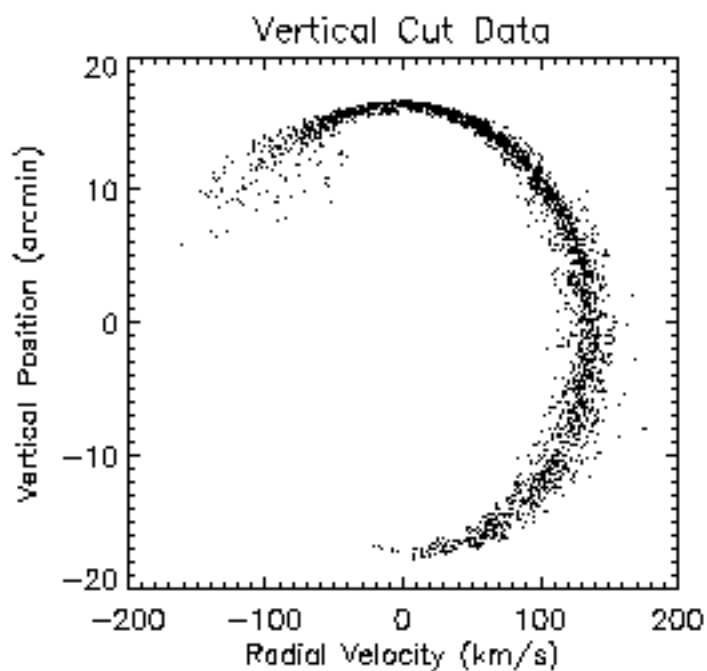
- A ejecta
- B hot x-ray emitting interior
- C cooler outer region of interior
- D active shell formation in equatorial band
- E cold dense shell, seen in recession in 21 cm, source of radio continuum, gamma rays, bounded by radiative shock
- F corrugation in shell, tangency seen as filament in radio continuum, H α , OH masers
- G shock with substantial cooling but no shell as yet
- H ambient medium with density gradient, lumpiness which corrugates shell
- I look direction



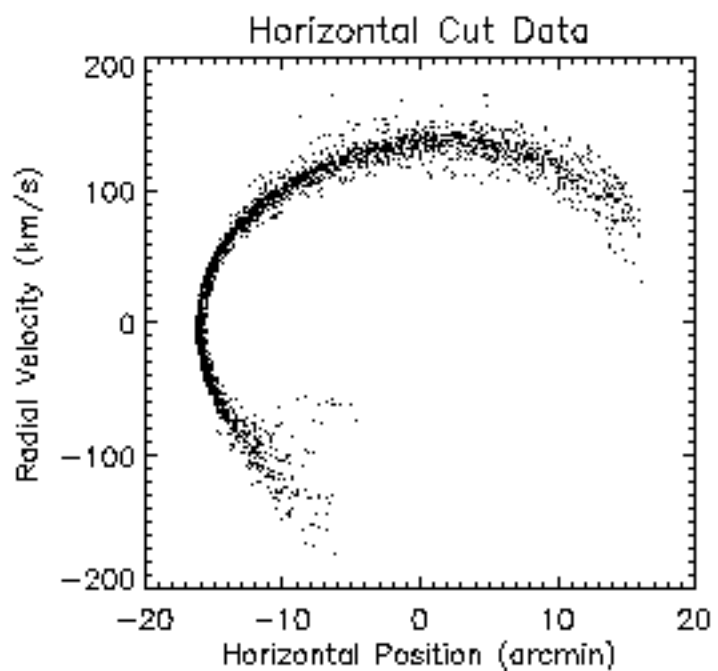
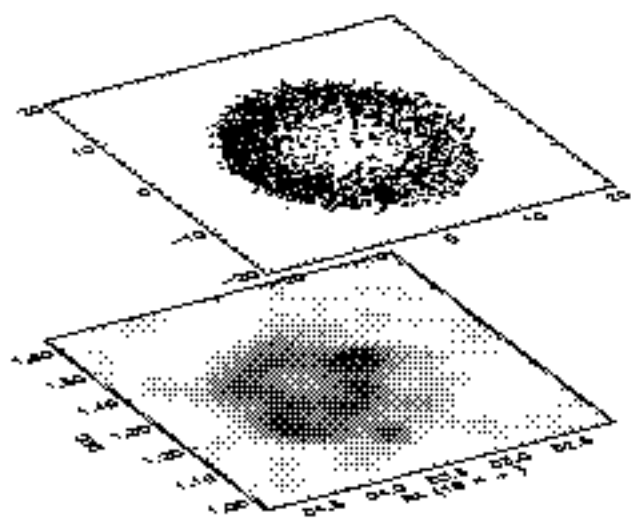


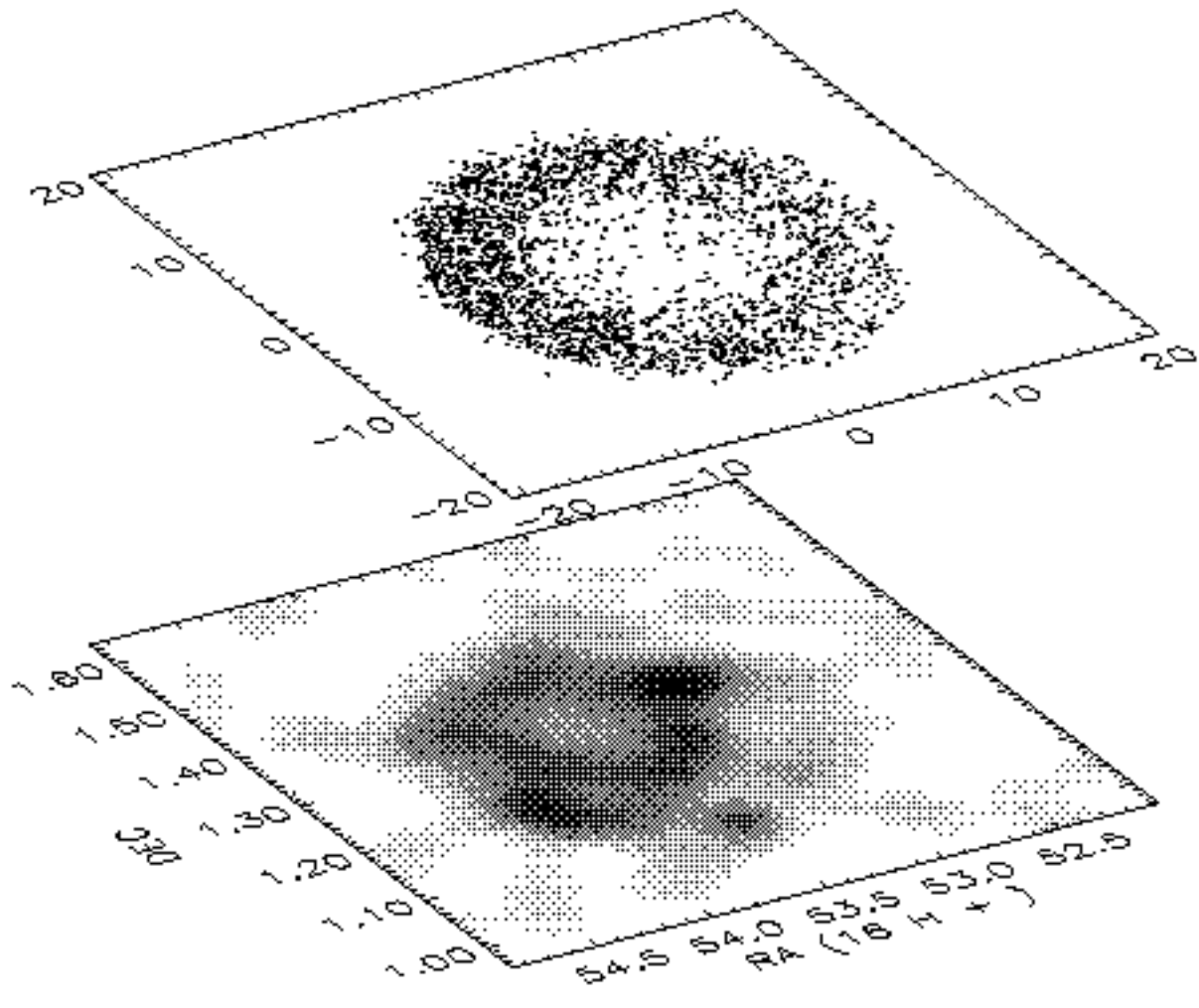


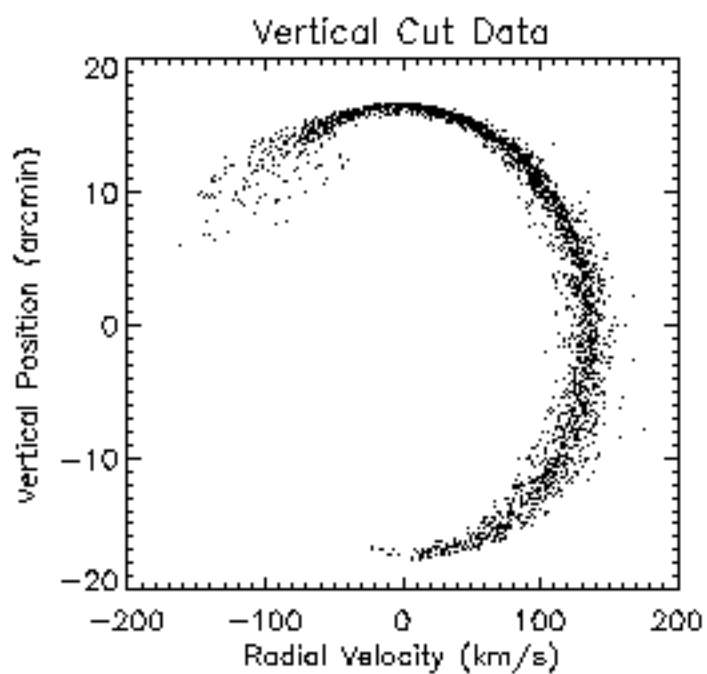




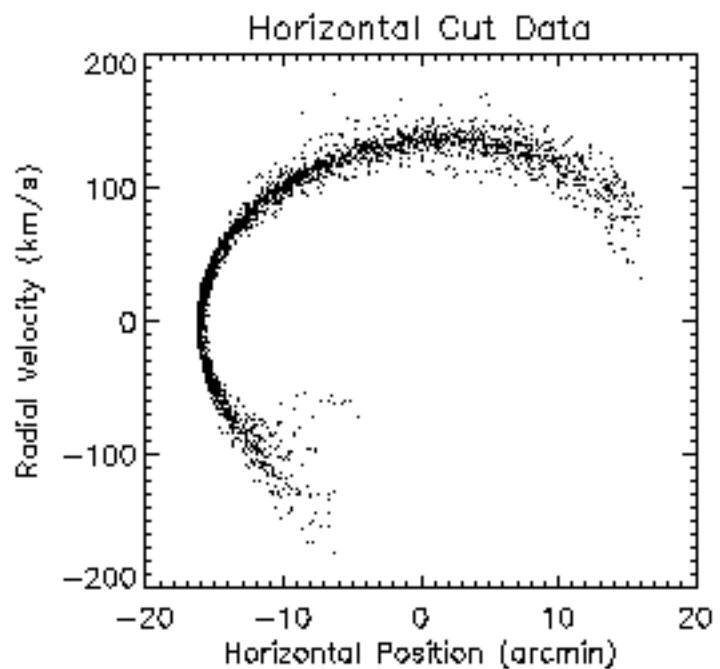
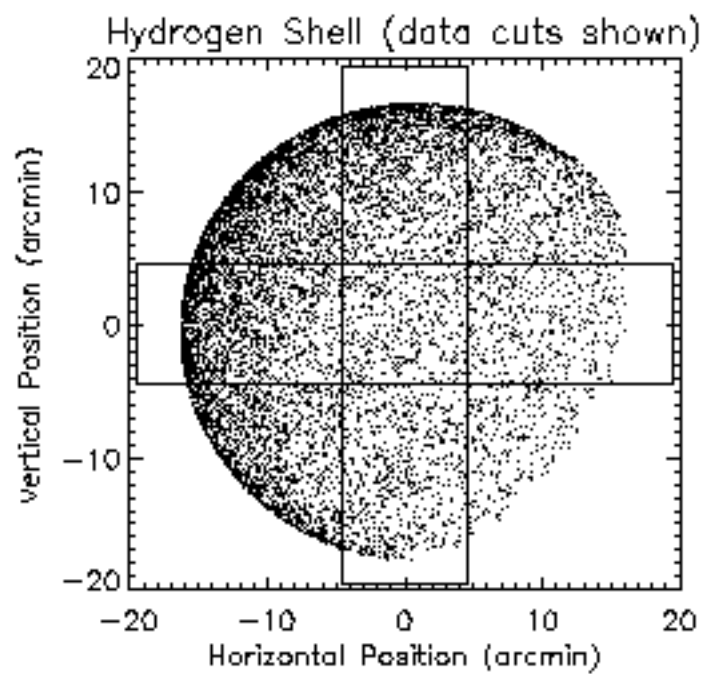
Shell in Limited Velocity Range

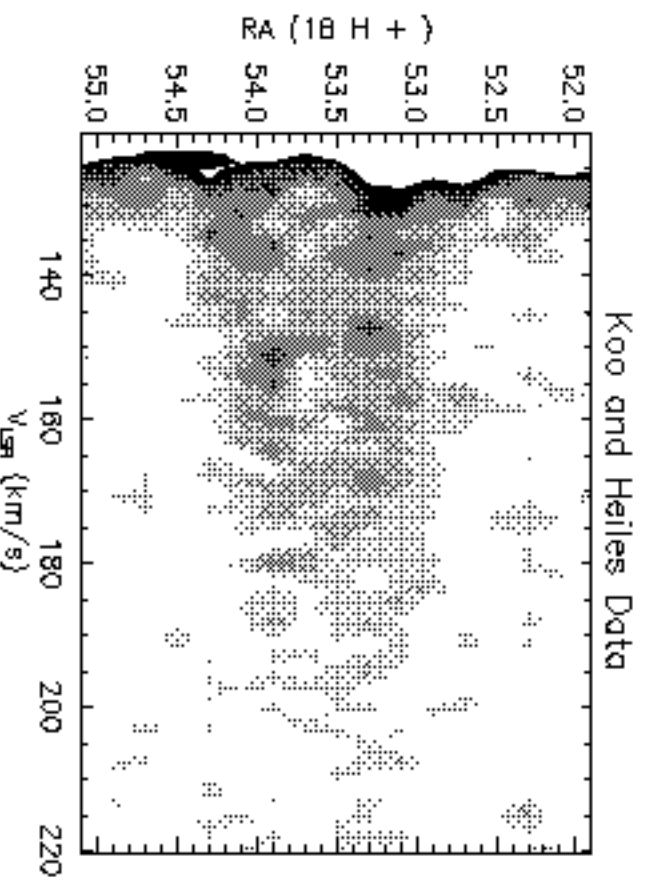
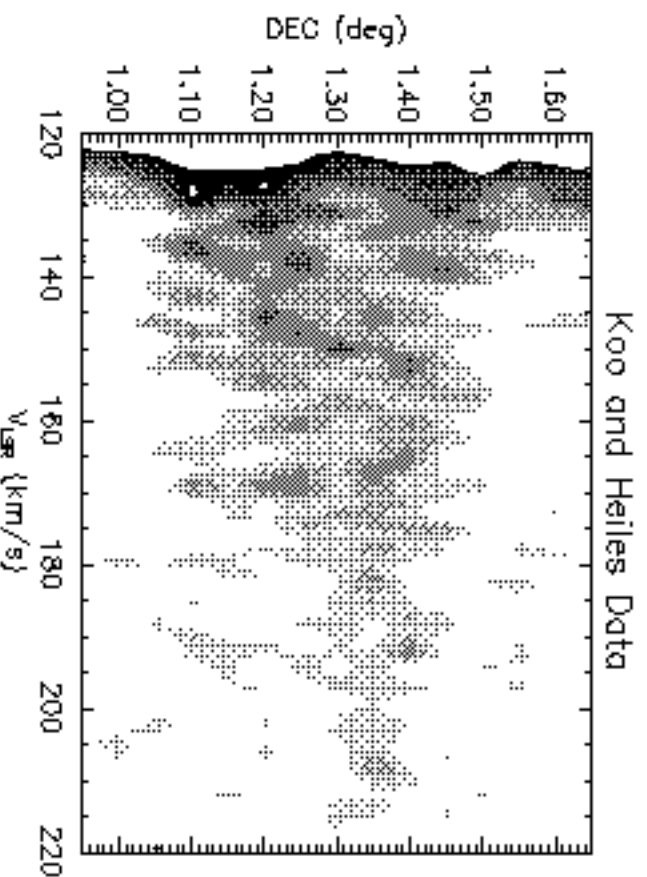
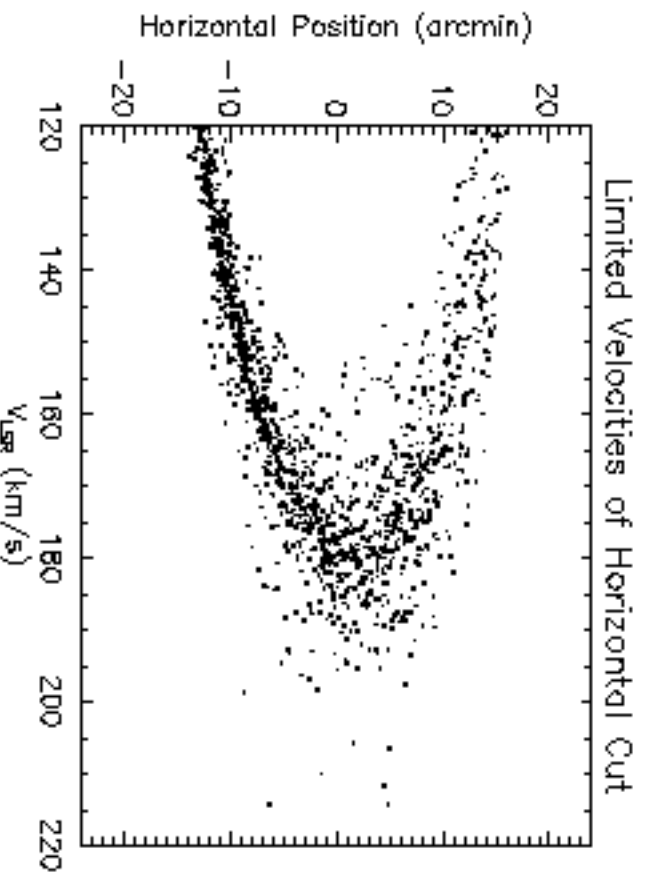
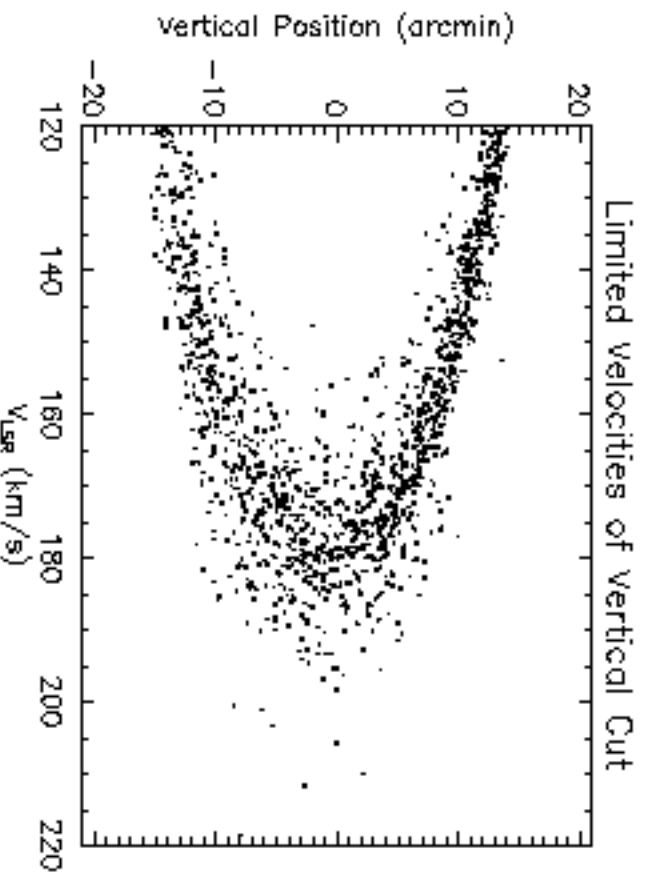


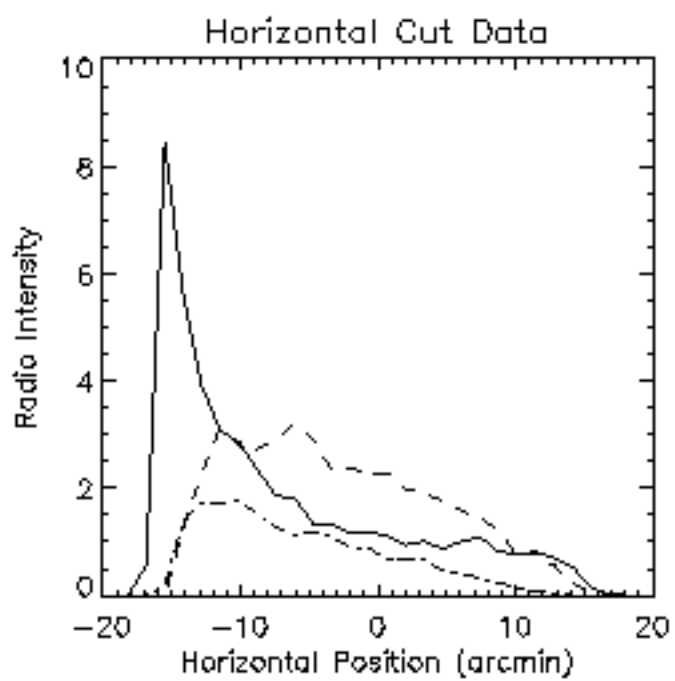
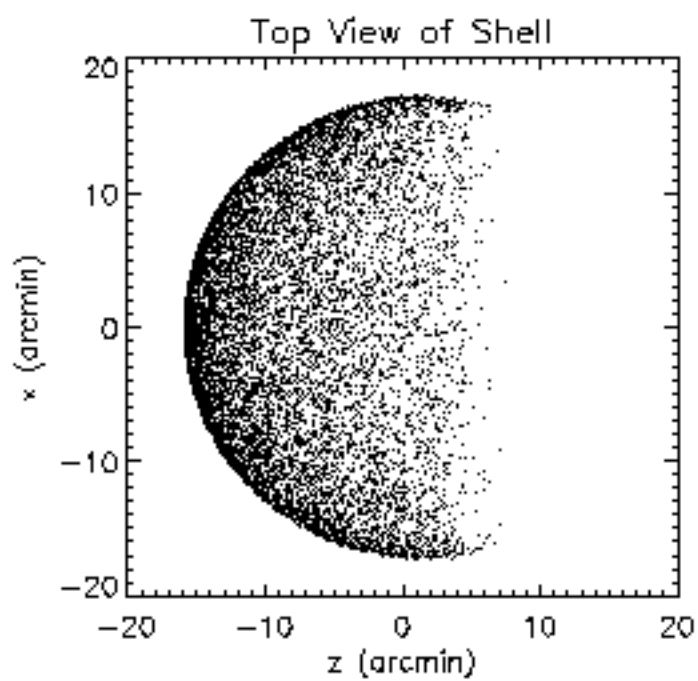
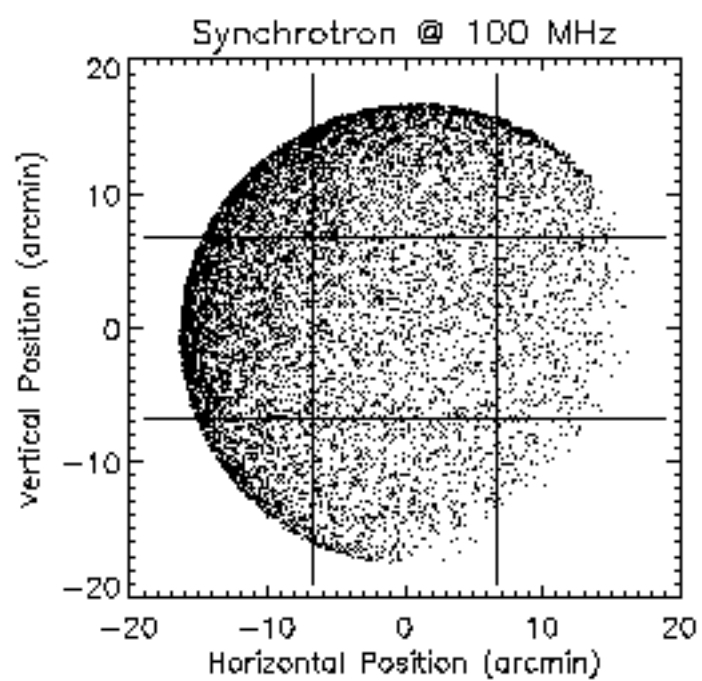
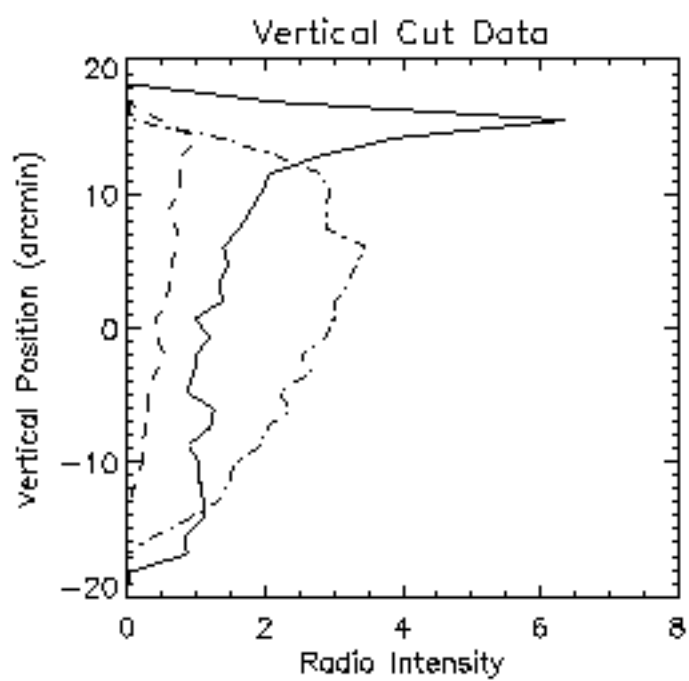


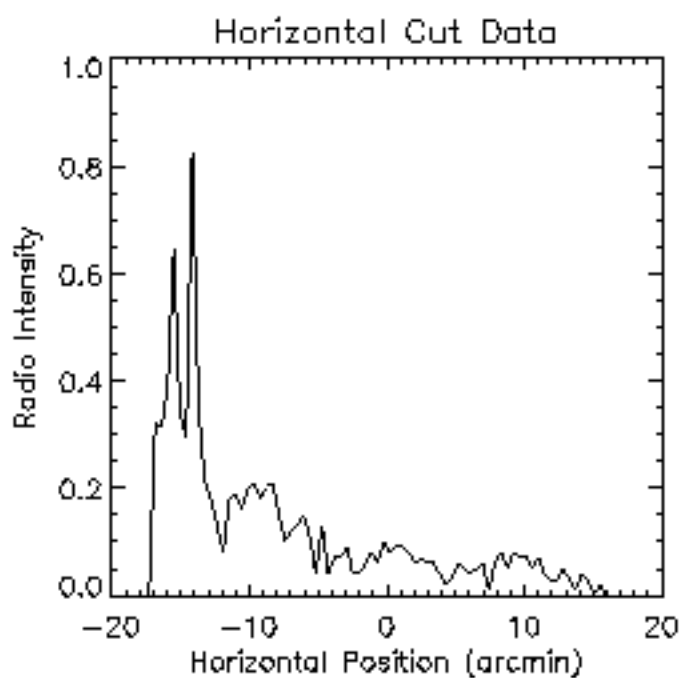
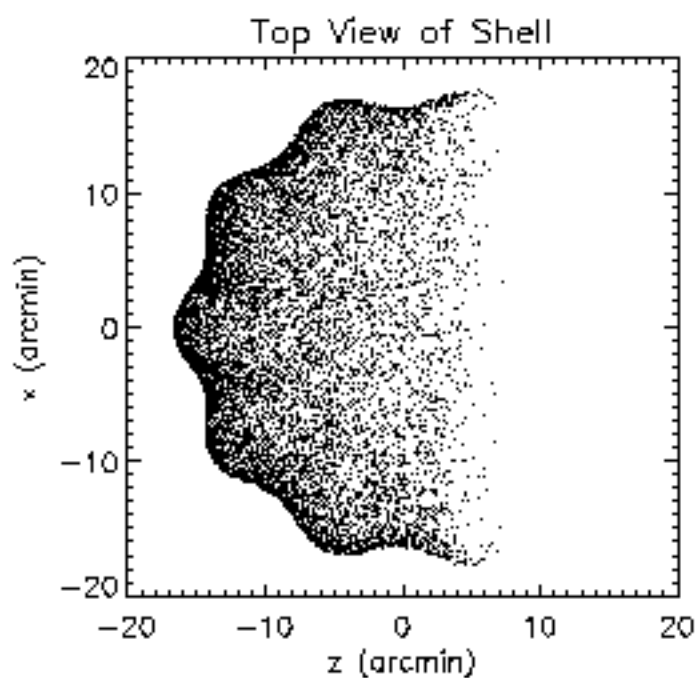
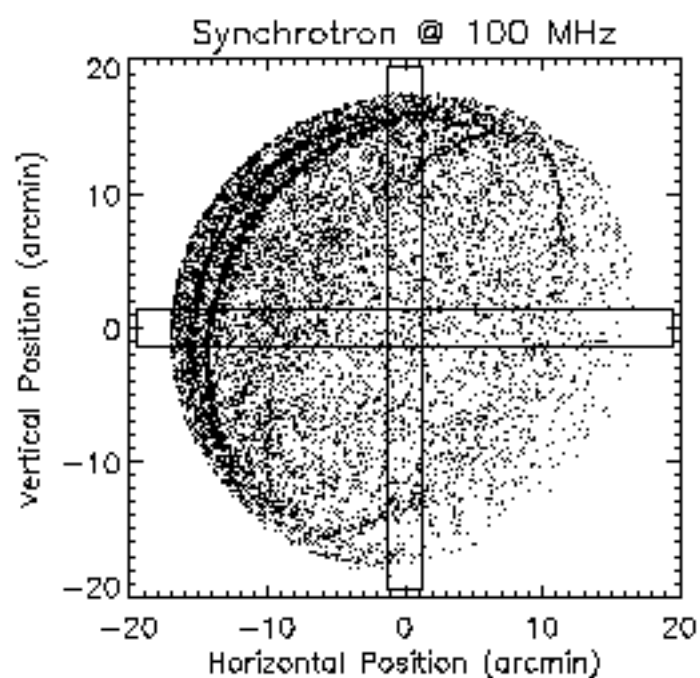
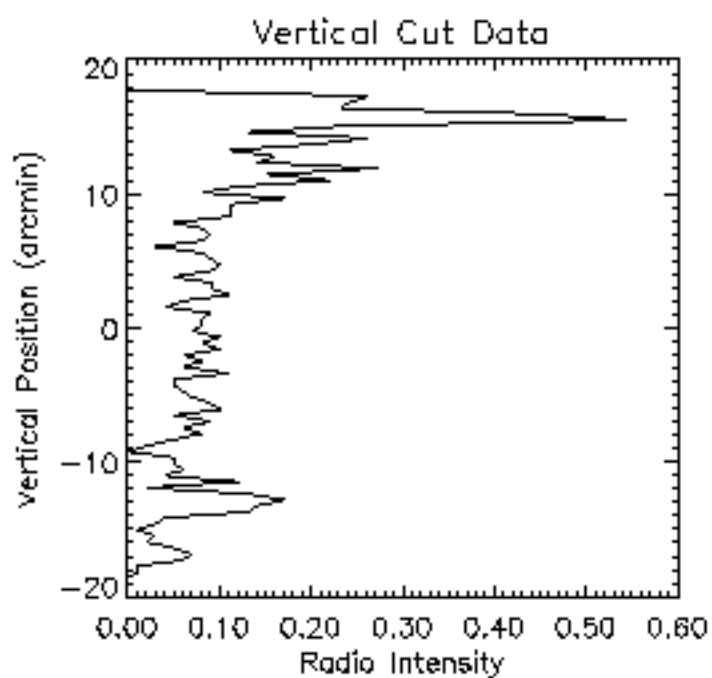


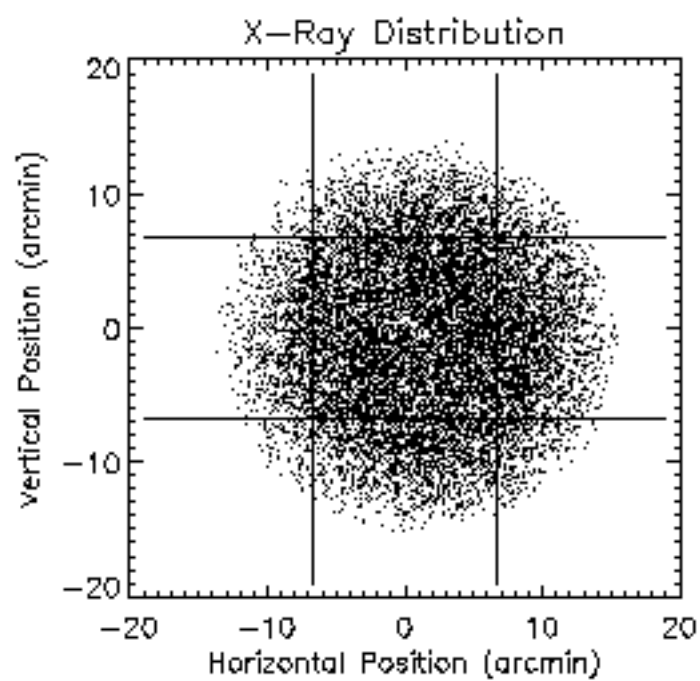
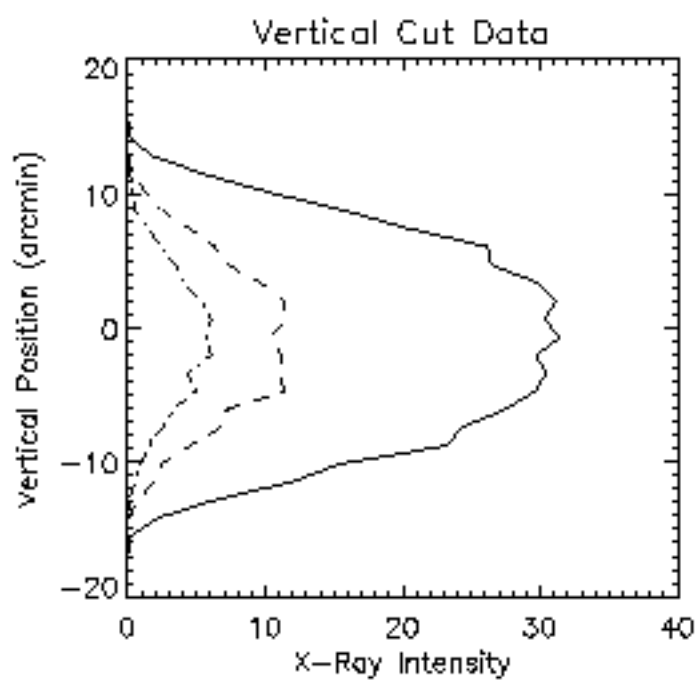
Shell in Limited Velocity Range



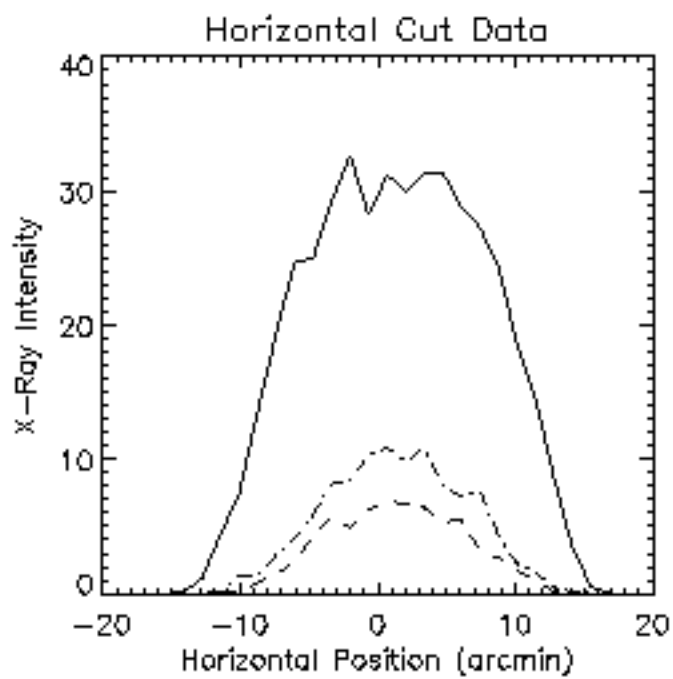


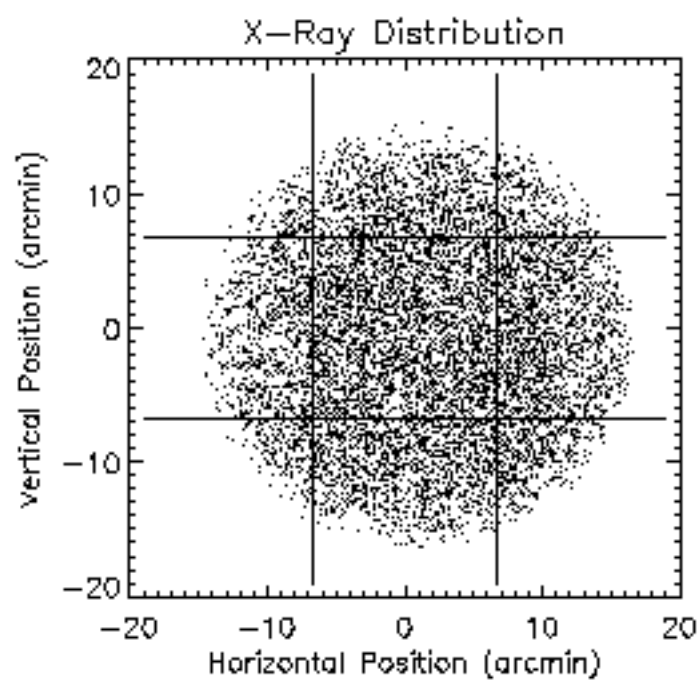
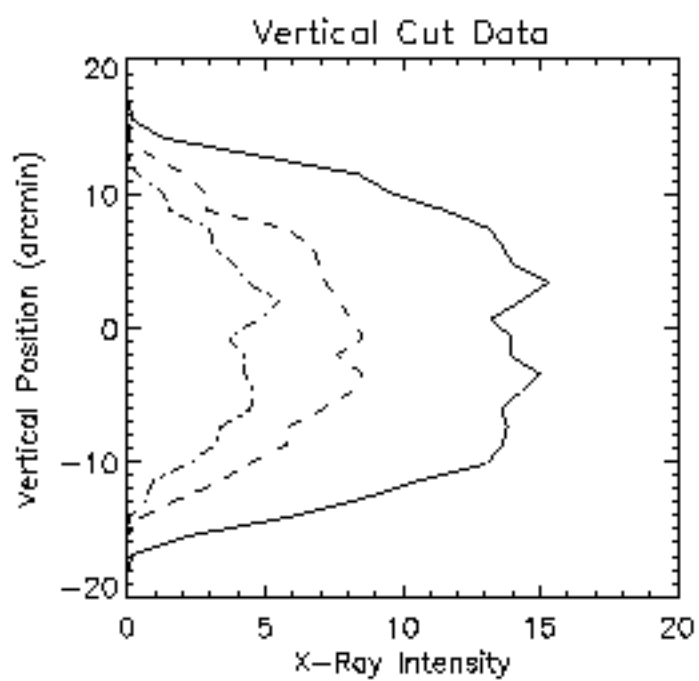






- . - . bottom/left cuts
—— middle cuts
- - - top/right cuts





. bottom/left cuts
 ————— middle cuts
 - - - - - top/right cuts

